Exponents for Hamiltonian paths on random bicubic maps and KPZ

Philippe Di Francesco[*1,2], Bertrand Duplantier[†1], Olivier Golinelli[‡1]
and Emmanuel Guitter[§1]

[1]Université Paris-Saclay, CEA, CNRS, Institut de physique théorique, 91191,
Gif-sur-Yvette, France
[2]Department of Mathematics, University of Illinois, Urbana, IL 61821, USA

October 18, 2022

We evaluate the configuration exponents of various ensembles of Hamiltonian paths drawn on random planar bicubic maps. These exponents are estimated from the extrapolations of exact enumeration results for finite sizes and compared with their theoretical predictions based on the KPZ relations, as applied to their regular counterpart on the honeycomb lattice. We show that a naive use of these relations does not reproduce the measured exponents but that a simple modification in their application may possibly correct the observed discrepancy. We show that a similar modification is required to reproduce via the KPZ formulas some exactly known exponents for the problem of unweighted fully packed loops on random planar bicubic maps.

1. Introduction

The aim of this paper is to evaluate a number of exponents characterizing the asymptotic enumeration of various configurations of Hamiltonian paths on random planar bicubic maps. Recall that a *planar map* is a connected graph drawn on the two-dimensional (2D) sphere (or equivalently on the plane) without edge crossings, and considered up to continuous deformations. A map is characterized by its vertices and edges, inherited

---

[*]philippe.di-francesco@ipht.fr

[†]bertrand.duplantier@ipht.fr

[‡]olivier.golinelli@ipht.fr
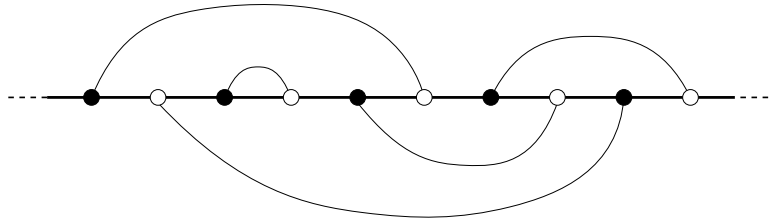
[§]emmanuel.guitter@ipht.fr

Figure 1: Representation of a (rooted) Hamiltonian cycle on a planar bicubic map as a system of non-crossing arches linking black and white vertices whose color alternate along a straight line.

from the underlying graph structure, and by its *faces* which result from the embedding and all have the topology of the disk. The map is called *bicubic* if (i) it is cubic, i.e., all its vertices have degree 3 (i.e., have 3 incident half-edges) and (ii) these vertices are colored in black and white so that any two adjacent vertices have different colors. A *Hamiltonian* path is a self-avoiding path along the edges of the map which visits all the vertices of the map. If the path is closed, it is called a *Hamiltonian cycle.*

The problem of Hamiltonian cycles on random bicubic maps was first considered in [1] where it was conjectured that its scaling limit corresponds to 2D quantum gravity coupled to a conformal field theory (CFT) with central charge $c = -1$. In particular, the number z_N of configurations of planar bicubic maps with $2N$ vertices endowed with a Hamiltonian cycle and a marked visited edge, called the *root* edge, was predicted in [1] to behave, at large N, as

$$z_N \sim \text{const.} \; \frac{\mu^{2N}}{N^{2-\gamma}} \tag{1}$$

with an exponential growth rate estimated numerically as $\text{Log}(\mu^2) \sim 2.313$ and with the somewhat nontrivial exponent

$$\gamma = -\frac{1 + \sqrt{13}}{6} \; . \tag{2}$$

By cutting the Hamiltonian cycle at the level of its root edge and stretching it into a straight line, a configuration may be drawn in the plane as a simple infinite line with $2N$ alternating black and white vertices, completed by non-crossing arches linking each black vertex to a white one, either above or below the infinite line, see Figure 1 for an example. Despite this simple representation, no exact expression for z_N or its asymptotic equivalent is known so far and the results of [1] remain mathematically a conjecture.

In the present paper, we address the question of evaluating a number of other exponents, similar to γ and characterizing more involved Hamiltonian path configurations with possible valency and/or occupation defects. In our study, we will be led to consider a generalization of the Hamiltonian cycle problem to the so-called FPL(n) model on bicubic maps, where FPL stands for *Fully Packed Loops.* Configurations of the FPL(n) model now consist of an arbitrary number of *loops* which are closed paths drawn along the edges of the underlying bicubic map, so that loops are both self- and mutually avoiding and each vertex of the map is visited by a loop. Each loop receives the weight n,

with n a real number between 0 and 2. Three values of n are of particular interest: the case $n = 2$ describes unweighted *oriented* loops, the case $n = 1$ that of unweighted loops, while taking the limit $n \to 0$ allows us to recover the original Hamiltonian cycle problem with a single loop.

A strategy to explore the asymptotics of Hamiltonian cycles, or more generally that of the FPL(n) model on random bicubic maps consists in using the general connection which links 2D conformal field theories in random geometry to their classical (Euclidean) counterpart via the so-called *KPZ formulas* [2]. These formulas act as a translation tool giving global configuration exponents for the random map problem from the value of the associated critical correlation exponents (also called classical dimensions) in the corresponding regular lattice problem. Note that this "KPZ strategy" was carried out successfully in [3] and [4] (see also [5]) to identify various configuration exponents for *meanders*, a related combinatorial problem with now *two* intertwined fully packed loops drawn on random tetravalent planar maps.

The regular infinite bicubic map is nothing but the honeycomb lattice. The FPL(n) model on the honeycomb lattice was considered in [6] and many exact results were obtained by various approaches such as Bethe Ansatz techniques [7] or more heuristic Coulomb Gas (CG) methods [8], see also [9]. We can therefore deduce from these results a number of KPZ-induced configuration exponents for the random map problem. In the case $n = 0$, we can then compare the predicted values for these exponents with their numerical estimates obtained from the extrapolation of *exact enumeration results for finite N*, as was done with success in [1] for the exponent γ above. As it will appear, the "naive" KPZ approach, based on a direct application of the KPZ formulas, does not lead to satisfactory results for $n = 0$. Still it seams that the observed mismatch with numerical estimates might be corrected if, before applying the KPZ formulas, we slightly modify the expression of the critical correlation exponents by a simple extra "normalization" procedure involving a single parameter α. As we shall see, a similar α-corrected KPZ procedure is required in the case $n = 1$ when comparing KPZ-induced configuration exponents to exactly known results for specific observables.

The paper is organized as follows: Section 2 presents a number of known results for the FPL(n) model on the honeycomb lattice: after recalling its Coulomb Gas description in Section 2.1, we give the expression for various critical exponents corresponding to vortex-antivortex correlations in Section 2.2. Specific examples of these correlations and their meaning in terms of loops are discussed in Section 2.3. We then turn in Section 3 to the coupling of the FPL(n) model to gravity. After discussing in Section 3.1 the specificity of bicubic maps in connection with foldable triangulations, we recall in Section 3.2 the general KPZ relations for the coupling to gravity of a 2D conformal theory. We also discuss in Section 3.3 the expected limits of both the standard O(n) model and the FPL(n) model in terms of Schramm-Loewner Evolution (SLE) and Liouville quantum gravity (LQG). We then use in Section 4 an equivalence between the FPL(1) model on bicubic maps and a particular instance of the 6-vertex model on tetravalent maps to obtain, in the case $n = 1$, the configuration exponents for a family of vortex-antivortex
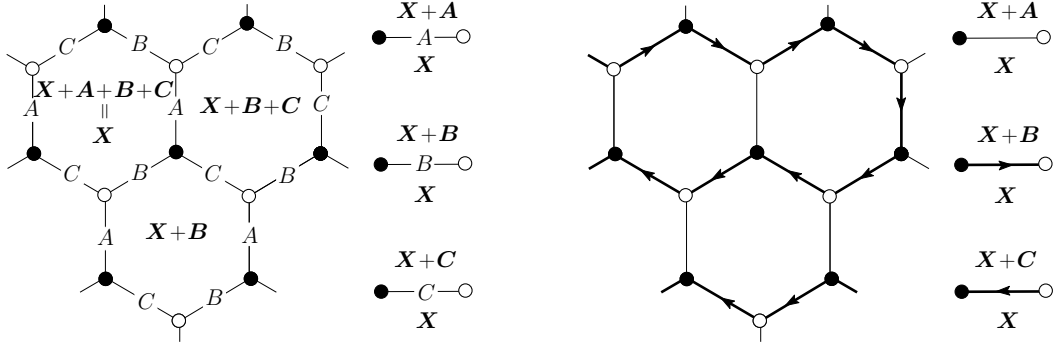
Figure 2: Left: an edge 3-coloring configuration of a portion of honeycomb lattice with colors A, B and C. Right: the associated configuration of fully packed oriented loops. The B- and C-colored edges form the oriented loops, while the A-edges correspond to the unvisited edges. For each representation, we indicated the variation of the 2D height variable $\boldsymbol{X}$ when crossing an edge.

correlations. We note that, quite surprisingly, the direct application of the KPZ formulas does not reproduce these results but that the observed discrepancy is easily cured in this case if we allow for a slight modification of the classical dimensions before applying the KPZ formulas. Our main results are presented in Sections 5 and 6: Section 5 deals with the exact numerical enumeration of configurations of Hamiltonian paths on bicubic maps with finite sizes and possible defects. After discussing in Section 5.1 our enumeration methods, we present in Section 5.2 our enumeration results for various ensembles of configurations with maximal sizes ranging from $N = 16$ up to $N = 28$. These results are then used in Sections 5.3 and 5.4 respectively to estimate the asymptotic exponential growth rate and the configuration exponent for each of the configuration ensembles at hand. The comparison with the KPZ predictions is then discussed in Section 6. Again we observe a mismatch with the numerical estimates and we present a tentative α-corrected KPZ procedure which seems to resolve this discrepancy. We gather a few remarks in Section 7. In particular, we explore the possible meaning of the parameter α. Appendix A discusses configuration exponents for Hamiltonian paths drawn on (non-necessarily bicolorable) planar cubic maps and shows the validity of the naive KPZ approach in this case. Appendix B presents the complete list of our exact enumeration results for the various Hamiltonian path configurations on bicubic maps that we have studied.

2. Coulomb Gas description of the FPL(n) model on the honeycomb lattice

2.1. General theory

Following [8], we start with the description of the FPL(2) model on the honeycomb lattice which, as discussed above, corresponds to configurations of fully packed oriented loops.
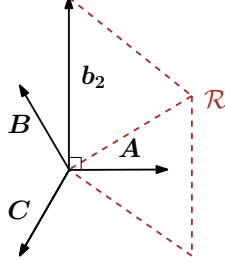
4

Figure 3: The two-dimensional vectors $\boldsymbol{A}$, $\boldsymbol{B}$, $\boldsymbol{C}$ and $\boldsymbol{b_2}$ and a portion of the $\mathcal{R}$ lattice.

As displayed in Figure 2, a configuration can be alternatively described as a 3-coloring of the edges of the lattice by colors A, B and C, so that the three edges incident to any vertex be of different colors. It is indeed easily seen that, for such a 3-coloring, the B- and C-colored edges form closed loops of alternating B- and C-edges visiting all the vertices of the lattice, while the A-edges correspond to the unvisited edges. Orienting the visited edges from their black to their white incident vertex for B-edges, and from their white to their black incident vertex for C-edges induces a well-defined orientation for each loop. Changing the orientation of a loop simply corresponds to interchanging the B- and C-edges along it.

We may finally transform the FPL(2) configurations into a "height-model" by assigning to each hexagonal face a *two-dimensional* height $\boldsymbol{X} \in \mathbb{R}^2$ whose variation $\Delta \boldsymbol{X}$ between neighboring faces depends on the nature of their separating edge, with the dictionary of Figure 2. In the 3-coloring language, we have $\Delta \boldsymbol{X} = \boldsymbol{A}$ (resp. $\boldsymbol{B}$, $\boldsymbol{C}$) if the crossed edge is of color A (resp. B, C) and traversed with the incident black vertex on the left. Making a complete turn around any vertex of the honeycomb lattice implies the constraint $\boldsymbol{A} + \boldsymbol{B} + \boldsymbol{C} = \boldsymbol{0}$ so that $\boldsymbol{X}$ is indeed two-dimensional.

Following [8], we make the following symmetric choice of vectors, see Figure 3:

$$\boldsymbol{A} := \left(\frac{1}{\sqrt{3}}, 0\right) , \quad \boldsymbol{B} := \left(-\frac{1}{2\sqrt{3}}, \frac{1}{2}\right) , \quad \boldsymbol{C} := \left(-\frac{1}{2\sqrt{3}}, -\frac{1}{2}\right) , \tag{3}$$

so that $|\boldsymbol{A}| = |\boldsymbol{B}| = |\boldsymbol{C}| = 1/\sqrt{3}$ and $\boldsymbol{A} \cdot \boldsymbol{B} = \boldsymbol{B} \cdot \boldsymbol{C} = \boldsymbol{C} \cdot \boldsymbol{A} = -1/6$. The height variable $\boldsymbol{X}$ takes its values within the triangular lattice $\mathcal{T} := \mathbb{Z}\boldsymbol{B} + \mathbb{Z}\boldsymbol{C}$, with mesh size $1/\sqrt{3}$. We also define the "repeat lattice" as the sub-lattice of $\mathcal{T}$ given by

$$\mathcal{R} := \mathbb{Z}(\boldsymbol{A} - \boldsymbol{B}) + \mathbb{Z}(\boldsymbol{A} - \boldsymbol{C}) \tag{4}$$

which is a triangular lattice of mesh size 1 (see Figure 3). It is such that two pieces of lattice whose values of the 2D height differ globally by an element of $\mathcal{R}$ describe the same coloring arrangement, hence the same loop configuration environment.

In [8], it is claimed that the model may then be described at large scale by a coarse-grained variable $\boldsymbol{\Psi}(x) = \langle \boldsymbol{X} \rangle$ suitably averaged in the vicinity of the point x of the underlying lattice, where $\boldsymbol{\Psi}$ is governed by the free field action

$$\mathcal{A}_{CG} = \pi g \int d^2 x \, (\nabla \boldsymbol{\Psi})^2 \tag{5}$$

with $g = 1$ (with our choice of normalization for $\boldsymbol{A}, \boldsymbol{B}, \boldsymbol{C}$). The variable $\boldsymbol{\Psi}$ is defined modulo $\mathcal{R}$, i.e., is an element of $\mathbb{R}^2/\mathcal{R}$ via the equivalence relation in $\mathbb{R}^2$:

$$\boldsymbol{\Psi} \equiv \boldsymbol{\Psi}' \iff \boldsymbol{\Psi} - \boldsymbol{\Psi}' \in \mathcal{R} . \tag{6}$$

Since the loops follow the B- and C-colored edges, the color A on the one hand and the colors B and C on the other hand play very different roles in the description of loop observables. It is then convenient to introduce the vector

$$\boldsymbol{b_2} := \boldsymbol{B} - \boldsymbol{C} = (0, 1) , \tag{7}$$

so that $|\boldsymbol{b_2}| = 1$ and $\boldsymbol{b_2} \cdot \boldsymbol{A} = 0$, and to work in the *orthogonal basis* $(\boldsymbol{A}, \boldsymbol{b_2})$, see Figure 3. We thus write

$$\boldsymbol{\Psi} = \psi_1 \boldsymbol{A} + \psi_2 \boldsymbol{b_2} . \tag{8}$$

For a fixed n ($0 \leq n \leq 2$), the wanted weight n per loop in the FPL(n) model is obtained by introducing *local weights* accounting for the left or right nature of the turns of the (oriented) loops at each vertex. At large scales, this new weight results into a modified Coulomb Gas action (see [8, 9] for details)

$$\mathcal{A}_{CG} = \int d^2x \left\{ \pi g \left(\frac{1}{3} (\nabla \psi_1)^2 + (\nabla \psi_2)^2 \right) + \frac{1}{2} \mathrm{i}\, e_0\, \psi_2\, R + : e^{4\mathrm{i}\pi\psi_2} : \right\} \tag{9}$$

where R is the (local) scalar curvature of the underlying lattice[1], and with now

$$g = 1 - e_0 = 1 - \frac{1}{\pi} \arccos\left(\frac{n}{2}\right) . \tag{10}$$

The last term in the action is the most relevant perturbation which allows one to fix g by demanding that it be marginal [9]. At this stage, it is important to note that the action is such that the two components ψ_1 and ψ_2 of the field $\boldsymbol{\Psi}$ are decoupled. The component ψ_1 along $\boldsymbol{A}$ is governed by a simple free field action, while the component ψ_2 along $\boldsymbol{b_2}$ is governed by a usual *one-dimensional* CG action, similar to that obtained from the SOS reformulation of a dense O(n) model (i.e., without the constraint that each vertex is visited by a loop). Still, a coupling between the two directions $\boldsymbol{A}$ and $\boldsymbol{b_2}$ arises when we deal with the operator spectrum of the FPL(n) model, as the defect configurations must be consistent with the condition (6). Finally, the central charge of the FPL(n) model on the honeycomb lattice is given by

$$c_{\mathrm{fpl}}(n) = 1 + c_{\mathrm{dense}}(n) = 2 - 6\frac{(1-g)^2}{g} \tag{11}$$

where, in the middle expression, the first term 1 is the central charge for the free scalar field ψ_1 and the second term is the usual central charge

$$c_{\mathrm{dense}}(n) = 1 - 6\frac{(1-g)^2}{g} \tag{12}$$

of a dense O(n) model (as obtained for instance from its one-dimensional CG description [10]). For $n = 0$ ($g = \frac{1}{2}$), this yields a total central charge $c_{\mathrm{fpl}}(0) = 1 - 2 = -1$.

---

[1]For instance, if the model is defined on a cylinder by taking periodic conditions in one direction, the scalar curvature is concentrated at both ends of the cylinder.

2.2. Exponents for vortex-antivortex correlations

The operator spectrum of the FPL(n) model on the honeycomb lattice is discussed in details in [8]. Of particular interest are the so-called *vortex operators* characterized, in the CG language, by their 2D *magnetic charge* $\boldsymbol{M} \in \mathcal{R}$. An operator with magnetic charge $\boldsymbol{M}$ corresponds to the insertion of a dislocation at a given lattice vertex, i.e., a topological defect $\delta \boldsymbol{X} = \boldsymbol{M}$ in the 2D height when going counterclockwise around that vertex. Several defects must be introduced simultaneously so that the total magnetic charge is zero (this guarantees that the 2D height remains well defined at infinity) to keep a finite free energy cost. For instance, the vortex-antivortex correlation corresponds to inserting a vortex of charge $\boldsymbol{M}$ and one of charge $-\boldsymbol{M}$ at two fixed vertices distant by r in the honeycomb lattice. For

$$\boldsymbol{M} = j(\boldsymbol{A} - \boldsymbol{B}) + k(\boldsymbol{A} - \boldsymbol{C}) \in \mathcal{R}, \quad j, k \in \mathbb{Z} , \tag{13}$$

the change ΔF of free energy induced by the introduction of the $\boldsymbol{M}/-\boldsymbol{M}$ defect is expected to behave at large r as $e^{-\Delta F} \sim r^{-4h_{\boldsymbol{M}}}$ with exponent [8]

$$h_{\boldsymbol{M}} = \frac{g}{4}\left(j^2 + k^2 + j\,k\right) - \frac{(1-g)^2}{4g}\left(1 - \delta_{j,k}\right) . \tag{14}$$

Using instead coordinates in the orthogonal basis $(\boldsymbol{A}, \boldsymbol{b_2})$, i.e., writing $\boldsymbol{M} = \frac{3}{2}(j+k)\boldsymbol{A} + \frac{1}{2}(k-j)\boldsymbol{b_2}$, we may recast the above result into

$$h_{\boldsymbol{M}} = \frac{g}{12}\phi_1^2 + \frac{g}{4}\left(1 - \delta_{\phi_2,0}\right)\left(\phi_2^2 - \left(1 - g^{-1}\right)^2\right) \qquad \text{for} \quad \boldsymbol{M} = \phi_1 \boldsymbol{A} + \phi_2 \boldsymbol{b_2} , \tag{15}$$

where the coordinates ϕ_1 and ϕ_2 are now integers or half-integers satisfying $\phi_1 \in \frac{3}{2}\mathbb{Z}$, $\phi_2 \in \frac{1}{2}\mathbb{Z}$ and $\phi_1 + \phi_2 \in \mathbb{Z}$. Note that, as a consequence of the decoupled form (9) of the action, the expression above for $h_{\boldsymbol{M}}$ is naturally split into two terms: a first contribution depending on the coordinate ϕ_1 along $\boldsymbol{A}$ only and a second contribution involving the coordinate ϕ_2 along $\boldsymbol{b_2}$ only.

2.3. Examples

Let us illustrate the result (15) in the case $n = 0$ and for a few values of the magnetic charge $\boldsymbol{M}$. For $n = 0$ $(g = \frac{1}{2})$, Equation (15) reduces to

$$h_{\boldsymbol{M}}(n = 0) = \frac{1}{24}\phi_1^2 + \frac{1}{8}\left(1 - \delta_{\phi_2,0}\right)\left(\phi_2^2 - 1\right) . \tag{16}$$

The case $\boldsymbol{M} = \boldsymbol{B} + 2\boldsymbol{A} = \frac{3}{2}\boldsymbol{A} + \frac{1}{2}\boldsymbol{b_2}$. A vortex with magnetic charge $\boldsymbol{B} + 2\boldsymbol{A}$ corresponds to a black vertex surrounded by two $\boldsymbol{A}$'s and one $\boldsymbol{B}$ which, in the loop language, corresponds to a black vertex from which a path originates (see Figure 4). The corresponding antivortex, of charge $-\boldsymbol{B} - 2\boldsymbol{A}$ corresponds to the end of this path at a further
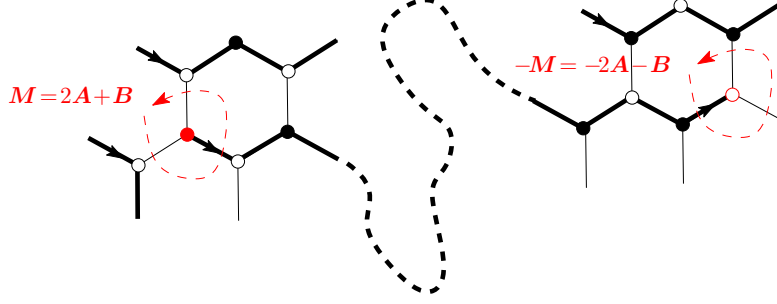
Figure 4: Schematic representation of a pair of defects with magnetic charges $\pm \boldsymbol{M}$ for $\boldsymbol{M} = 2\boldsymbol{A}+\boldsymbol{B}$ in the case of arbitrary n. This corresponds to fully packed loop configurations containing an open oriented path starting at a black vertex and ending at a white one. If these vertices are at distance r apart from each other on the honeycomb lattice, the change ΔF of free energy due to the defects is expected to behave as $e^{-\Delta F} \sim r^{-4h_{\boldsymbol{M}}}$.
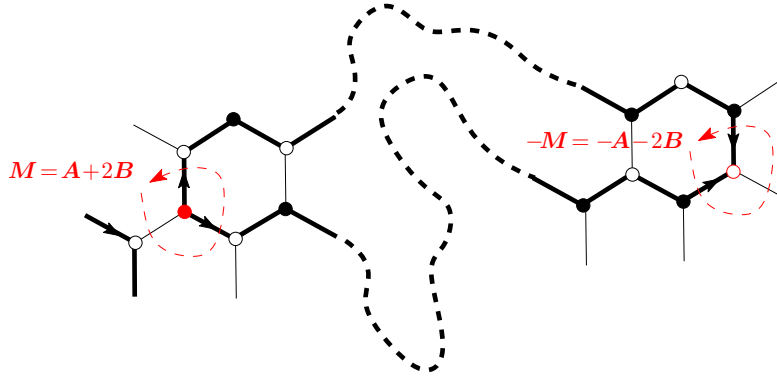

Figure 5: Schematic representation of a pair of defects with magnetic charges $\pm \boldsymbol{M}$ for $\boldsymbol{M} = \boldsymbol{A}+2\boldsymbol{B}$ in the case of arbitrary n. This corresponds to fully packed loop configurations with two open oriented paths starting at a black vertex and meeting again at a (black or white) vertex at distance r apart.

apart white vertex. For $n \to 0$, this vortex-antivortex correlation therefore enumerates configurations with a single *open* path which is fully packed, i.e., visits all the vertices of the lattice, and with prescribed (black) starting and (white) ending points at distance r from each other. From (16), we have

$$h_{\boldsymbol{B}+2\boldsymbol{A}}(n = 0) = \frac{1}{24}\left(\frac{3}{2}\right)^2 + \frac{1}{8}\left(\left(\frac{1}{2}\right)^2 - 1\right) = 0 \ , \tag{17}$$

meaning that the free energy cost induced by having remote endpoints for the path tends to a constant for large r. A possible explanation for this result is that, for $n \to 0$, the length of the Hamiltonian path joining the defects is independent of r and depends only on the size of the underlying lattice.
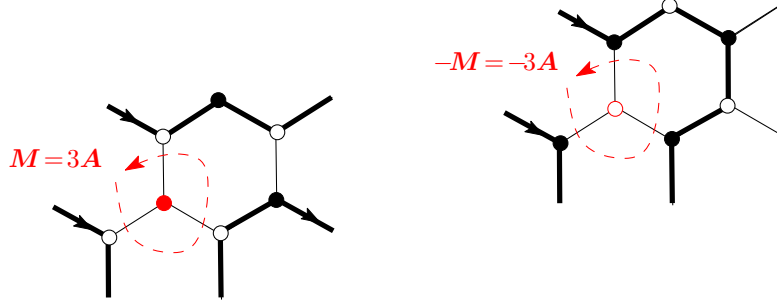
Figure 6: Schematic representation of a pair of defects with magnetic charges $\pm M$ for $M = 3A$. This corresponds to fully packed loop configurations with two unvisited vertices, one of each color, at given distant r from each other.

The case $M = A + 2B = b_2$. A vortex with magnetic charge $A + 2B$ corresponds to two paths originating from the same black vertex (see Figure 5), and ending at the white vertex[2] where we put the antivortex $-A - 2B$. By changing the orientation of one of the paths, the concatenation of the two paths forms a well-oriented loop: the vortex-antivortex correlation therefore enumerates fully packed loop configurations for which two prescribed vertices on the honeycomb lattice at distance r from each other belong to the *same* loop. For $n \to 0$, this is always the case since the configuration is made of a single cycle. This is consistent with the value

$$h_{A+2B}(n = 0) = \frac{1}{8}\left((1)^2 - 1\right) = 0 . \tag{18}$$

The case $M = 3A$. This corresponds to having a black and a white vertex at distance r apart which are not visited by a loop. For $n \to 0$, we then have a unique fully packed loop visiting all vertices but two (see Figure 6). We find

$$h_{3A}(n = 0) = \frac{1}{24}(3)^2 = \frac{3}{8} , \tag{19}$$

meaning that the number of configurations decays as $r^{-3/2}$ at large r. Since $h_{3A} < 1$, such a defect corresponds to a relevant perturbation. This agrees with the fact that the fully packed loop fixed point (here for $n = 0$) is unstable with respect to the creation of "empty" vertices: giving these vertices a finite chemical potential drifts the model toward a new fixed point, that of the dense O(n) model, with central charge $c_{\text{dense}}(n)$ as in (12) [10].

---

[2]We may also put the antivortex at a black vertex, now with magnetic charge $A + 2C$ so that the total charge is $A + 2B + A + 2C = 0$.

3. Coupling to gravity

3.1. A word on bicubic maps

The vertices of the honeycomb lattice all have degree 3. As such, the honeycomb lattice may be viewed as the regular lattice associated with random *cubic* maps. However, as opposed to the honeycomb lattice, an arbitrary cubic map is not vertex bicolorable in general. The existence of a bicoloring of the vertices in black and white was crucial when defining the 2D height X coding for a fully packed (oriented) loop configuration. Without this coloring, it is not possible to distinguish between the two sides of an unvisited edge: this forces us to set $A = 0$ and $B = -C$ accordingly, leading to a height X which is one-dimensional only. A similar reduction of the dimension from 2 to 1 occurs on the honeycomb lattice itself if we allow for the presence of unvisited vertices with a finite chemical potential, as it imposes $3A = 0$. The corresponding "densely packed" $O(n)$ model is much simpler than the FPL(n) model and corresponds to a conformal theory of central charge $c_{\text{dense}}(n)$ as in (12), with g as in (10), which can be described at large scales by standard one-dimensional CG techniques [10]. The FPL(n) model, when defined on arbitrary random cubic maps, is therefore expected to be described by a conformal theory of reduced central charge $c = c_{\text{dense}}(n)$ coupled to gravity. For $n = 0$, this yields $c = -2$, a result which can directly be verified by an exact enumeration of the configurations (see Appendix A).

To get a non-trivial FPL(n) model with the augmented central charge $c_{\text{fpl}}(n)$ of (11), we therefore need to impose that the vertices of the random cubic map be *bicolored*, namely that the random map be *bicubic*. Planar bicubic maps are dual to planar *Eulerian triangulations*, i.e., maps whose all faces are triangles, colored in black and white so that no two adjacent faces have the same color. A necessary and sufficient condition for such a coloring to exist is that each vertex of the triangulation has even degree, which is also the condition for the map to be drawable without lifting the pen, starting and ending at the same vertex. This explains the denomination Eulerian. More interestingly, Eulerian triangulations are exactly those triangulations which, when made of *equilateral triangles* of fixed size (say, with all edge lengths equal to $1/\sqrt{3}$) can be embedded into the plane, keeping each triangle equilateral [5]. Any such embedding corresponds to what can be called a two-dimensional *folded* state of the triangulation and, in this sense, planar Eulerian triangulations are exactly those planar triangulations which are foldable in the plane (see Figure 7).

Consider now the FPL(2) model on random planar bicubic maps: as before, it is equivalent to a 3-coloring of the edges of the map in colors A, B and C so that each (trivalent) vertex is incident to edges of different colors. We can again define up to global translation a 2D height variable X on each face of the map, according to the rules of Figure 2, and with A, B and C as in Figure 3. Moreover, each 3-coloring corresponds to a specific folded state of the dual Eulerian triangulation and the 2D variable X, attached to the faces of the bicubic map, hence to the vertices of the triangulation, can be interpreted as the (two-dimensional) position of the associated triangulation vertex in the folded state [5], see Figure 7.
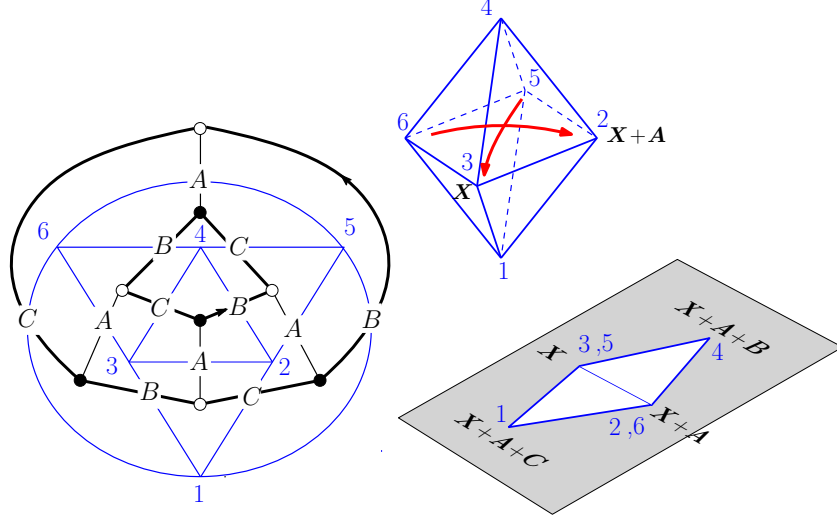
Figure 7: An example of bicubic map (black thick lines) with 3-colored edges and the dual Eulerian triangulation (blue thin lines), with the topology of an octahedron (upper right). The 3-coloring encodes a folded state of this octahedron in the plane as shown (lower right): the 2D height $\boldsymbol{X}$ associated with the 3-coloring is nothing but the position in the plane of the vertices of the octahedron after folding.

As in Section 2.2, we will consider configurations with magnetic defects $\boldsymbol{M}$ corresponding to unvisited vertices (e.g., for $\boldsymbol{M} = 3\boldsymbol{A}$), or vertices from which several lines emerge (e.g., for $\boldsymbol{M} = 2\boldsymbol{A} + \boldsymbol{B}$ or $\boldsymbol{M} = \boldsymbol{A} + 2\boldsymbol{B}$). An important difference between the random and regular cases is that we will not impose that the vertices carrying a defect be trivalent. We will for instance consider univalent unvisited vertices (defect $\boldsymbol{M} = \pm\boldsymbol{A}$) or open paths with univalent endpoints (defect $\boldsymbol{M} = \pm\boldsymbol{B}$ or $\pm\boldsymbol{C}$), and more generally m-valent defects with arbitrary positive integers m. As a consequence, the set of magnetic charges $\boldsymbol{M}$ is no longer restricted to the lattice $\mathcal{R}$ but is extended to the larger set $\mathcal{T} = \mathbb{Z}\boldsymbol{B} + \mathbb{Z}\boldsymbol{C}$. Writing as before $\boldsymbol{M} = \phi_1 \boldsymbol{A} + \phi_2 \boldsymbol{b_2}$, i.e. working in the $(\boldsymbol{A}, \boldsymbol{b_2})$ basis, we may now take $\phi_1 \in \frac{1}{2}\mathbb{Z}$ (instead of $\frac{3}{2}\mathbb{Z}$), $\phi_2 \in \frac{1}{2}\mathbb{Z}$ with still the constraint that $\phi_1 + \phi_2 \in \mathbb{Z}$.

3.2. The KPZ relations

The continuum description of the coupling of 2D quantum gravity to critical matter theories involves incorporating fluctuations of the underlying metric $\hat{g}$, which is deformed by a multiplicative local conformal factor $e^{\gamma_{\mathrm{L}}\varphi_{\mathrm{L}}}$, in terms of a scalar field φ_{L} governed by the Liouville action [11, 12]. For the coupling to gravity of a conformal field theory with central charge c, the parameter γ_{L} is fixed to the value

$$\gamma_{\mathrm{L}} = \gamma_{\mathrm{L}}(c) = \frac{1}{\sqrt{6}}\left(\sqrt{25 - c} - \sqrt{1 - c}\right) \in (0, 2] \quad \text{for} \quad c \in (-\infty, 1]\,, \tag{20}$$

by requiring that the (regularized) Liouville random measure $d^2 x : e^{\gamma_{\mathrm{L}}\varphi_{\mathrm{L}}(x)} :$ is conformally invariant. The matter is now subject to the fluctuations of the metric, and in

11

particular matter fields acquire a multiplicative gravitational dressing of the form $e^{\alpha_{\mathrm{M}}\varphi_{\mathrm{L}}}$ for a suitable value of the "charge" α_{M}.

Correlation functions of dressed matter fields are also summed over fluctuations of the metric, hence positions of the fields are also integrated over in the process. However, correlators still depend on invariants of the random surfaces generated by the fluctuations of the metric, such as the *area*, given by $A = \int d^2x \sqrt{|\hat{g}|} : e^{\gamma_{\mathrm{L}}\varphi_{\mathrm{L}}(x)} :$ and the Einstein action, reduced to the Euler characteristic $\chi = \frac{1}{4\pi} \int d^2x \sqrt{|\hat{g}|}\, R = 2 - 2G$ by the Gauss-Bonnet formula, where R is the scalar curvature and G is the genus of the fluctuating surface.

In particular, the coupling of a CFT with central charge c to 2D quantum gravity on surfaces of fixed genus G and area A results in a new micro-canonical partition function behaving for large A as $Z_{A,G} \sim \text{const.}\ \mu^A\, A^{(\gamma(c)-2)\chi/2-1}$ in terms of the "string susceptibility exponent" $\gamma = 1 - 4/\gamma_{\mathrm{L}}^2$ [2, 11, 12], namely

$$\gamma = \gamma(c) = \frac{1}{12}\left(c - 1 - \sqrt{(1-c)(25-c)}\right)\ . \tag{21}$$

The parameter $\mu = e^\Lambda$ is related to the critical cosmological constant Λ, the chemical potential for the area term in the action. Note that for planar (genus zero) surfaces, this gives

$$Z_{A,0} \sim \text{const.}\ \mu^A\, A^{\gamma(c)-3}\ . \tag{22}$$

Likewise, dressed matter conformal primary fields $\Phi_{h,c}$ with classical dimension (or conformal weight) h acquire a gravitational anomalous dimension [2]

$$\Delta(h,c) = \frac{\sqrt{1-c+24\,h} - \sqrt{1-c}}{\sqrt{25-c} - \sqrt{1-c}}\ , \tag{23}$$

such that non-trivial gravitational p-point correlators on random surfaces (of fixed genus) obey the KPZ scaling:

$$\langle \prod_i \Phi_{h_i,c} \rangle_A \sim \text{const.}\ A^{\sum_i \{1-\Delta(h_i,c)\}}\ . \tag{24}$$

To make contact with our combinatorial problem, we wish to evaluate the large N scaling behavior of various loop models on random planar (bi)cubic maps with $2N$ vertices. We therefore set $G = 0$. We interpret $2N = A$ as a measure of the area (i.e., total number of triangles) of the corresponding discretized dual (triangulated) random surface. In the case of Hamiltonian cycles (see Figure 1), our object of interest has a marked root edge (or vertex) where we open the loop. The choices of this marking correspond to an overall factor of $2N = A$ and we expect therefore a scaling behavior for the partition function of rooted Hamiltonian cycles of the form $z_N = A\, Z_{A,0} \sim \text{const.}\ \mu^A\, A^{\gamma(c)-2}$. As indicated above, the bicubic nature of the graph ensures that the flat space matter degrees of freedom (the colors A, B, C) still describe the gravitational version of the model, which keeps the *same* central charge c in (21), with $c = c_{\mathrm{fpl}}(n)$ as in (11). For $n = 0$, we have seen that $c_{\mathrm{fpl}}(0) = -1$ and we recover the asymptotics (1) with the exponent $\gamma = \gamma(-1)$ given by (2).

In the following we will compute a number of 2 or 3-point correlators in the discrete model and estimate numerically the corresponding scaling behavior (i.e., both the values of μ and of the configuration exponents), which we will compare to the theoretical prediction (24), easily rewritten in the present case as

$$Z_{A,0} \langle \prod_i \Phi_{h_i,c} \rangle_A \sim \text{const. } \mu^A A^{\sum_i \{1-\Delta(h_i,c)\}+\gamma(c)-3} . \qquad (25)$$

As an illustration of the method, we describe in detail in Appendix A the exact computation of the scaling behavior of Hamiltonian cycles on cubic (not necessarily bicolorable) maps, and check the agreement with KPZ scaling at $c = c_{\text{dense}}(0) = -2$.

3.3. Scaling limits

It is widely believed that the *scaling limit* of the critical $O(n)$ model in two dimensions is described by the celebrated *Schramm-Loewner evolution* SLE_κ [13], and, more precisely, its collection of critical loops by the so-called *conformal loop ensemble* CLE_κ [14]. This conformally invariant random process depends on a single parameter $\kappa \geq 0$, which in the $O(n)$ model case is $\kappa = 4/g$, with $n = -2\cos(\pi g)$, and $g \in [1/2, 1)$, $\kappa \in (4, 8]$ for the *dense* critical phase, and $g \in [1, 3/2]$, $\kappa \in [8/3, 4]$ for the *dilute* critical phase [14, 15, 16, 17]. (We restrict ourselves here to $n \geq 0$, thus $\kappa \in [8/3, 8]$, the range for which CLE_κ is defined.) SLE_κ paths, which are always non self-crossing, are *simple*, i.e., non-intersecting when $\kappa \in [8/3, 4]$, and *non-simple* when $\kappa \in (4, 8]$ [18]. The associated SLE_κ central charge is then

$$c = c_{\text{sle}}(\kappa) := \frac{1}{4}(6 - \kappa)\left(6 - \frac{16}{\kappa}\right) \in [-2, 1] \quad \text{for} \quad \kappa \in [8/3, 8] . \qquad (26)$$

This scaling limit has been rigorously established in several cases: the contour lines of the discrete Gaussian free field, for which $n = 2, g = 1, \kappa = 4$ [19]; critical site percolation on the honeycomb lattice [20], for which $n = 1, g = 2/3, \kappa = 6$; the critical Ising model and its associated Fortuin-Kasteleyn random cluster model on the square lattice [21, 22] for which, respectively, $n = 1, g = 4/3, \kappa = 3$ and $n = \sqrt{2}, g = 3/4, \kappa = 16/3$.

The fully-packed $\text{FPL}(n)$ model stays in the *same universality class* as the corresponding dense $O(n)$ model, even though its central charge is shifted by one unit as in (11) (12). One reason is that the so-called *watermelon* exponents for an *even* number of paths are the same in $\text{FPL}(n)$ and $O(n)$ models [6, 7, 8], and in particular the 2-leg exponent which gives the Hausdorff dimension of the paths. One is thus led to conjecture that the scaling limit of the fully-packed $\text{FPL}(n)$ model on the honeycomb lattice is described by *space-filling* SLE_κ [23], with κ corresponding to the dense $O(n)$ model phase,

$$\kappa = \frac{4\pi}{\arccos(-n/2)} \in (4, 8] \quad \text{for} \quad n \in [0, 2) . \qquad (27)$$

In the $\text{FPL}(n = 0)$ case, one has $g = 1/2, \kappa = 8$, so its scaling limit should be given by SLE_8 (or CLE_8), which is a *Peano curve*, that is space-filling.

Random planar maps, as weighted by the partition functions of critical statistical models, are widely believed to have for scaling limits Liouville quantum gravity (LQG) coupled to the CFT describing these models, or, equivalently, to the corresponding SLE processes. Let us now recall two distinct results associated with the KPZ perspective [2].

The first KPZ relation (23) can be rewritten with the help of the Liouville parameter (20) as the simple quadratic formula,

$$h(\Delta) = \frac{\gamma_{\mathrm{L}}^2}{4}\Delta^2 + \left(1 - \frac{\gamma_{\mathrm{L}}^2}{4}\right)\Delta \ . \tag{28}$$

Its rigorous proof [24, 25, 26, 27] rests on the sole assumption that the Liouville field φ_{L} and (any) random fractal curve (possibly described by a CFT) are *independently* sampled.

The second KPZ result (21) for $\gamma(c)$ [2], or equivalently (20) for $\gamma_{\mathrm{L}}(c)$, gives the precise coupling between the LQG and CFT or SLE parameters. By substituting the SLE central charge $c = c_{\mathrm{sle}}(\kappa)$ of (26), one indeed obtains the simple expressions

$$\gamma = 1 - \sup\{4/\kappa, \kappa/4\}, \quad \gamma_{\mathrm{L}} = \inf\{\sqrt{\kappa}, \sqrt{16/\kappa}\} \ . \tag{29}$$

This has been rigorously established in the probabilistic approach by coupling the Gaussian free field in Liouville quantum gravity with SLE martingales [28, 29]. In the scaling limit, random cluster models on random planar maps can then be shown to converge (in the so-called peanosphere topology of the mating of trees perspective) to LQG-SLE [30].

This *matching* property (29) of γ, γ_{L} and κ applies to the scaling limit of the critical, dense or dilute, $O(n)$ model on a random planar map, as well as to the fully-packed FPL(n) model on random cubic maps. However, on *bicubic* maps, the correspondence (29) no longer holds, and one then has a *mismatch* [31], with $c = c_{\mathrm{sle}}(\kappa)$ of (26) replaced in (20), (21) and (23) by $c = c_{\mathrm{fpl}}(n) = 1 + c_{\mathrm{sle}}(\kappa)$, with κ still given by (27). Note that the constraint $c \leq 1$ in the KPZ relations restricts the loop fugacity of the FPL(n) model on a bicubic map to the range $n \in [0, 1]$ with $\kappa \in [6, 8]$, while the complementary range $n \in (1, 2)$ with $\kappa \in (4, 6)$ is likely to correspond to random tree statistics.

A coupling between LQG and space-filling SLE with such mismatched parameters has yet to be described rigorously. We can simply predict here that for $n \in [0, 1]$ the scaling limit of the FPL(n) model on a bicubic planar map will be given by space-filling SLE$_\kappa$, with $\kappa \in [6, 8]$ as in (27), on a γ_{L}-LQG sphere with Liouville parameter

$$\gamma_{\mathrm{L}} = \frac{1}{\sqrt{12}}\left(\sqrt{3\left(\kappa + \frac{16}{\kappa}\right) + 22} - \sqrt{3\left(\kappa + \frac{16}{\kappa}\right) - 26}\right) \ , \tag{30}$$

in agreement with conjectures proposed in [31].

For the FPL$(n = 0)$ model in the bicubic case, we have $\gamma_{\mathrm{L}} = \frac{1}{\sqrt{3}}\left(\sqrt{13} - 1\right)$, as opposed to $\gamma_{\mathrm{L}} = \sqrt{2}$ in the cubic case, whereas for the bicubic FPL$(n = 1)$ model, to which the next section is devoted, we have $\gamma_{\mathrm{L}} = 2$, instead of $\gamma_{\mathrm{L}} = \sqrt{8/3}$ in the cubic case.

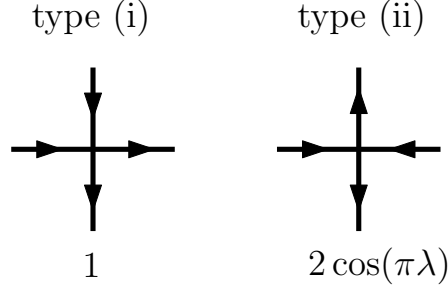type (i)   type (ii)

1                 $2\cos(\pi\lambda)$

Figure 8: The two types of vertex environments for the 6V model on a tetravalent map and the corresponding weights.

type (i)

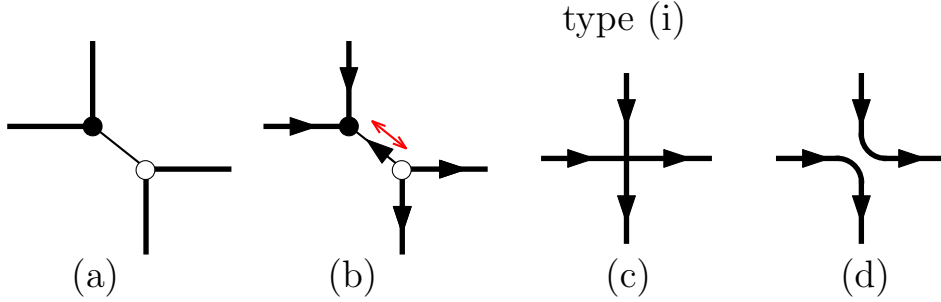(a)   (b)   (c)   (d)

Figure 9: In a bicubic map endowed with an unoriented fully packed loop configuration, we consider the pairs of black and white vertices linked by an unvisited edge (a). After orienting all incident edges away from the white vertex and towards the black one (b), we squeeze the unvisited edge so as to produce a tetravalent vertex of type (i) as shown in (c). Doing that for all pairs leads to a 6V configuration on a tetravalent map, where all the vertices are of type (i). The construction is clearly reversible. The 6V configuration may itself be transformed into a particular oriented fully packed loop configuration on the tetravalent map by untying the type (i) vertices as shown in (d).

4. Exponents for the FPL(1) model on bicubic maps

As we shall now see, a direct test of the KPZ formulas for the FPL(n) model on bicubic maps can be performed in the case $n = 1$, whose central charge, given by (11) with $g = 2/3$, is equal to $c = c_{\mathrm{fpl}}(1) = 1$. Indeed, as shown in [32], the FPL(1) model defined on planar bicubic maps is equivalent to a particular instance of the 6-vertex (6V) model on tetravalent planar maps.

We recall that the 6V model on tetravalent planar maps consists in orienting each edge of the map by an arrow, with the so-called *ice rule* that each vertex of the map is incident to exactly two (half-) edges carrying an incoming arrow and two (half-) edges carrying an outgoing arrow, see Figure 8. On a random tetravalent lattice, we may then distinguish between two vertex environments: for type (i) vertices, the two incoming arrows follow each other when turning around the vertex while for type (ii) vertices, they are separated by one outgoing arrow (see Figure 8). Given some fixed $\lambda \in [0, 1]$ we attach a weight
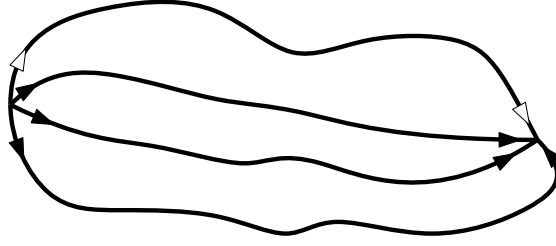
Figure 10: Schematic picture of the topology of oriented 6V loops in a watermelon configuration. We have here $\ell = 4$ paths, one of which is distinguished (white arrow).

$2\cos(\pi\lambda)$ to type (ii) vertices and 1 to type (i). In particular, for $\lambda = \frac{1}{2}$, the configurations of arrows with a non-zero weight are those where all the vertices are of type (i). These latter configurations are in bijection with those of the FPL(1) model on bicubic maps through the following correspondence: recall that $n = 1$ corresponds to the case of fully packed *unoriented* loops without any attached weight. For any such configuration, let us orient each edge of the underlying bicubic map from its white extremity to its black one. Note that this orientation is a property of the bicubic map only and is independent of its loop content. Now we may squeeze each *unvisited* edge by collapsing its two (black and white) extremities into a single, uncolored vertex of degree 4 (see Figure 9). By doing so, we build a tetravalent map with oriented edges (corresponding to all the edges originally visited by the loops) and such that each vertex is of type (i). The correspondence is one-to-one since we can put back the unvisited edge by splitting each type (i) vertex into a black and a white connected vertex by pulling the two incident incoming edges on one side (defining the black vertex) and the two incident outgoing edges on the other side (defining the white vertex), and finally remove all the arrows.

The 6V model on tetravalent planar maps with an arbitrary $\lambda \in [0, 1]$ was studied in detail by random matrix techniques [33, 34] where, as expected, it was shown to correspond to a $c = 1$ CFT coupled to gravity. The arrow configurations of the 6V model may themselves be transformed into fully packed oriented loop configurations on the underlying tetravalent maps by "untying" the vertices (see Figure 9-(d) in the case of a type (i) vertex). Note that these oriented loops are different from the (unoriented) loops of the associated FPL(1) model (these latter loops would correspond instead to paths along which 6V arrow orientations alternate). In the 6V loop language, one may then consider the *watermelon* configurations, with two defects: a source from which ℓ oriented lines emerge and a sink at which they all end, see Figure 10. The corresponding configuration exponent Δ_ℓ was computed exactly with the result [34, Eq. (4.26) with $\lambda = 1/2$]:

$$\Delta_\ell = \frac{\ell}{8} \ . \tag{31}$$

Let us now try to recover this result from the general KPZ formulas (21) and (25) in the original FPL(1) language. In this language, the source (respectively sink) defects corresponds to an unvisited black (respectively white) vertex as shown in Figure 11. More precisely, for even ℓ, the unvisited black vertex has degree $\ell/2$ and thus corresponds to a
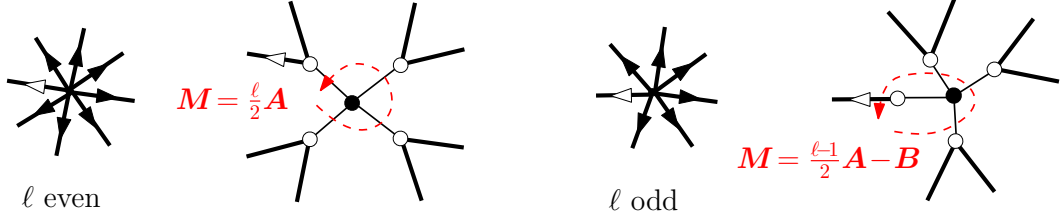
Figure 11: Correspondence between a source of ℓ lines in the $6V$ model and an unvisited black vertex of degree $\lceil\frac{\ell}{2}\rceil$ in the FPL(1) model. The associated magnetic charge $\boldsymbol{M}$ accounting for the 2D height defect is equal to $\frac{\ell}{2}\boldsymbol{A}$ for even ℓ and to $\frac{\ell-1}{2}\boldsymbol{A} - \boldsymbol{B}$ for odd ℓ.

defect with magnetic charge $\boldsymbol{M} = \frac{\ell}{2}\boldsymbol{A}$. For odd ℓ, the unvisited black vertex is connected to $(\ell-1)/2$ regular white trivalent vertices and to a final white bivalent vertex so that the total magnetic charge of the defect is now $\boldsymbol{M} = \frac{\ell-1}{2}\boldsymbol{A} - \boldsymbol{B} = \frac{\ell}{2}\boldsymbol{A} - \frac{1}{2}\boldsymbol{b_2}$. For $n = 1$ ($g = \frac{2}{3}$), Equation (15) becomes

$$h_{\boldsymbol{M}}(n = 1) = \frac{1}{18}\phi_1^2 + \frac{1}{6}\left(1 - \delta_{\phi_2,0}\right)\left(\phi_2^2 - \frac{1}{4}\right) \ . \tag{32}$$

In particular, we get

$$
\begin{aligned}
h_{\frac{\ell}{2}\boldsymbol{A}}(n = 1) &= \frac{1}{18}\left(\frac{\ell}{2}\right)^2 = \frac{\ell^2}{72} \qquad \text{for } \ell \text{ even} , \\
h_{\frac{\ell}{2}\boldsymbol{A}-\frac{1}{2}\boldsymbol{b_2}}(n = 1) &= \frac{1}{18}\left(\frac{\ell}{2}\right)^2 + \frac{1}{6}\left(\left(-\frac{1}{2}\right)^2 - \frac{1}{4}\right) = \frac{\ell^2}{72} \qquad \text{for } \ell \text{ odd} ,
\end{aligned}
\tag{33}
$$

hence a result $h_\ell = \frac{\ell^2}{72}$, independently of the parity of ℓ.

For $c = 1$, the KPZ relation (23) simplifies into $\Delta(h, 1) = \sqrt{h}$. Applying this relation leads us to predict a configuration exponent for the watermelon configuration equal to:

$$\Delta(h_\ell, 1) = \frac{\ell}{6\sqrt{2}} \ . \tag{34}$$

This value disagrees with the exact value (31), meaning that the direct application of the KPZ formula *does not yield the correct result*.

There is however a simple procedure allowing us to cure the observed discrepancy: let us define

$$h_{\boldsymbol{M}}^{(\alpha)} := \alpha\frac{g}{12}\phi_1^2 + \frac{g}{4}\left(1 - \delta_{\phi_2,0}\right)\left(\phi_2^2 - \left(1 - g^{-1}\right)^2\right) \qquad \text{for} \quad \boldsymbol{M} = \phi_1\boldsymbol{A} + \phi_2\boldsymbol{b_2} , \tag{35}$$

which mimics the expression (15) for $h_{\boldsymbol{M}}$ by introducing an extra normalization factor α in front of the first term (i.e., that depending on the component ϕ_1 in the direction

17

$\boldsymbol{A}$) with no modification of the second term (i.e., that depending on the component ϕ_2 in the direction $\boldsymbol{b_2}$). We observe immediately that

$$
\begin{aligned}
h^{(\alpha)}_{\frac{\ell}{2}\boldsymbol{A}}(n=1) &= \frac{\alpha}{18}\left(\frac{\ell}{2}\right)^2 = \frac{\alpha\,\ell^2}{72} \qquad \text{for } \ell \text{ even }, \\
h^{(\alpha)}_{\frac{\ell}{2}\boldsymbol{A}-\frac{1}{2}\boldsymbol{b_2}}(n=1) &= \frac{\alpha}{18}\left(\frac{\ell}{2}\right)^2 + \frac{1}{6}\left(\left(-\frac{1}{2}\right)^2 - \frac{1}{4}\right) = \frac{\alpha\,\ell^2}{72} \qquad \text{for } \ell \text{ odd },
\end{aligned}
\tag{36}
$$

leading again to the same value $h^{(\alpha)}_\ell = \frac{\alpha\,\ell^2}{72}$ for both parities. In particular, choosing $\alpha = 9/8$ leads to

$$
\Delta(h^{(9/8)}_\ell, 1) = \sqrt{h^{(9/8)}_\ell} = \frac{\ell}{8} = \Delta_\ell \ .
\tag{37}
$$

Otherwise stated, the KPZ relation leads to the correct result provided that we change the exponent $h_{\boldsymbol{M}}$ into the modified exponent $h^{(\alpha)}_{\boldsymbol{M}}$ with $\alpha = 9/8$, where the modification $h_{\boldsymbol{M}} \to h^{(\alpha)}_{\boldsymbol{M}}$ affects only the part of $h_{\boldsymbol{M}}$ depending on the component of $\boldsymbol{M}$ along $\boldsymbol{A}$ in the $(\boldsymbol{A}, \boldsymbol{b_2})$ basis, with no modification of the part of $h_{\boldsymbol{M}}$ depending on the component of $\boldsymbol{M}$ along $\boldsymbol{b_2}$. In other words, the compactification radius of the ϕ_1 component must be renormalized multiplicatively.

This new recipe might seem *ad hoc* but let us make a few comments about it. In the action (9), we decided to attach the *same* "stiffness" g to both directions ψ_1 and ψ_2 of the field $\boldsymbol{\Psi}$ (the $1/3$ factor is only there to correct the fact that $\boldsymbol{A}$ and $\boldsymbol{b_2}$ have different norms). This isotropic choice is natural for $n = 2$, which describes the pure 3-coloring problem where all colors play the same role but one might question its validity for $n < 2$. A crucial step which led to the expression (14), or equivalently (15) for the dimension $h_{\boldsymbol{M}}$ was then the ability to determine the value (10) for this isotropic stiffness g. As discussed in [8], one way to fix this value is to demand that the "electric" operator with smallest charge in the action (9) (the $: e^{4i\pi\psi_2} :$ term) be marginal. Strictly speaking however, since this criterion involves only the second coordinate ψ_2, it only fixes the stiffness in the ψ_2 direction, leaving that in the ψ_1 direction to some undetermined value g' since, as already mentioned, the two directions ψ_1 and ψ_2 are totally independent. On the honeycomb lattice, it seems that $g' = g$ is the correct choice since the values $h_{\boldsymbol{M}}$ (15) obtained by [8] match with those obtained by Bethe Ansatz methods [7]. It may however occur that, when coupled to gravity, the effective stiffness g' takes a different value with a ratio $\alpha := g'/g \neq 1$ due to metric fluctuations. If so, this would precisely modify $h_{\boldsymbol{M}}$ into $h^{(\alpha)}_{\boldsymbol{M}}$ within the KPZ formula. Verifying this hypothesis would require to be able to couple the CG formalism to the fluctuating Liouville field φ_{L} within a unified quantum field theory for the three fields ψ_1, ψ_2 and φ_{L} and to repeat the KPZ arguments in this formalism. Still, we present in Section 7 a tentative interpretation of the selected value $\alpha = 9/8$ for $n = 1$.

5. Numerics for $n = 0$

5.1. Enumeration methods

We wish to perform the exact enumeration of Hamiltonian path configurations on planar bicubic maps with a finite number $2N$ of vertices and with possible magnetic defects. To this end, we use the arch representation displayed in Figure 1 or suitable modifications thereof to account for the desired defects. In all cases, the Hamiltonian path is deformed into a straight line with alternating black and white vertices and we must complete it with non-crossing arches above or below the line connecting vertices of distinct colors. We used two different "orthogonal" enumeration approaches which we describe now.

The transfer matrix method   The first approach is a transfer matrix method where we build the arch configurations from left to right along the straight line of alternating black and white vertices. A configuration is described by the sequence of colors of those arches which have been open but not yet closed: each arch inherits the color of the vertex it originates from, see Figure 12. We read the upper arch sequence from bottom to top and, if it is made of p arches with colors $a_1, \ldots, a_p$ (with $a_i = 1$ for black and 0 for white), we code it via the integer $n_u = 2^p + \sum_{i=1}^{p} a_i 2^{(i-1)}$. Similarly, the lower arch sequence read from top to bottom gives a positive integer n_d, so that the intermediate state may be written as $|n_u, n_d\rangle$. In this setting, the empty configuration corresponds to the state $|1, 1\rangle$ and the number of configuration z_N may be written as

$$z_N = \langle 1, 1|(T_\circ T_\bullet)^N|1, 1\rangle \tag{38}$$

with the two elementary transfer matrices $T_\bullet$ and $T_\circ$ defined via

$$\langle n_u', n_d'|T_\bullet|n_u, n_d\rangle = \delta_{n_u', 2n_u+1}\delta_{n_d', n_d} + \delta_{n_u', n_u}\delta_{n_d', 2n_d+1} + \delta_{n_u', \frac{n_u}{2}}\delta_{n_d', n_d} + \delta_{n_u', n_u}\delta_{n_d', \frac{n_d}{2}}$$

$$\langle n_u', n_d'|T_\circ|n_u, n_d\rangle = \delta_{n_u', 2n_u}\delta_{n_d', n_d} + \delta_{n_u', n_u}\delta_{n_d', 2n_d} + \delta_{n_u', \frac{n_u-1}{2}}\delta_{n_d', n_d} + \delta_{n_u', n_u}\delta_{n_d', \frac{n_d-1}{2}} \ . \tag{39}$$

This expression allows us to enumerate z_N up to $N = 28$ (see Table 2) and this approach can be adapted to situations with (magnetic) defects.

The up-down factorization method   This second approach is closer in spirit to that of [1] and is based on a *two-step* construction process of Hamiltonian cycles, see Figure 13. The first step consists in assigning an up or down orientation to each of the $2N$ vertices drawn along the straight line. The second step consists in connecting all the up (resp. down) vertices by bicolored (i.e., with endpoints of different colors) arches drawn above (resp. below) the infinite line. The interest of the method is the following: once the vertex orientations have been fixed, the system of "up" arches and that of "down" arches are totally *independent* and the counting of Hamiltonian cycles is therefore entirely factorized. Moreover, the method is very flexible and it is more easily adaptable to the case with defects than its transfer matrix counterpart.
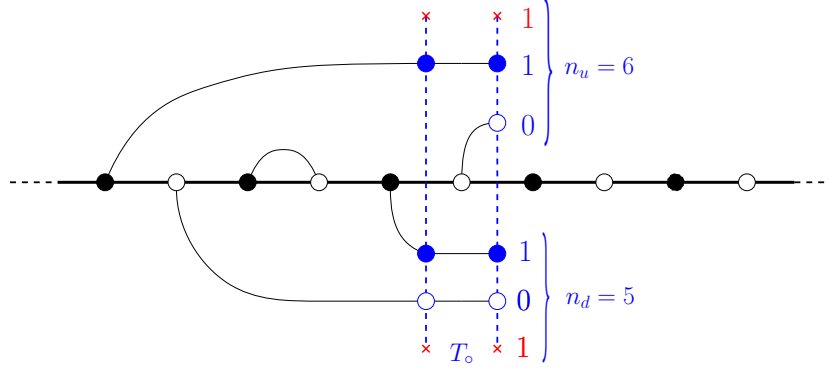
Figure 12: Illustration of the transfer matrix method. The arch configuration is built from left to right: each intermediate state (here along a blue dashed line) is coded by two positive integers n_u and n_d. The passage from one intermediate state to the next corresponds to the action of $T_\circ$ (as shown here) or $T_\bullet$ alternatively along the line.

More precisely, the $2N$ vertices are numbered by integers v from 1 to $2N$ according to their position along the straight line, say from left to right. The color $\mathrm{col}(v)$ of the vertex v is nothing but its parity $\mathrm{col}(v) = v \bmod 2$ (with the convention that $\mathrm{col} = 0$ for white and $\mathrm{col} = 1$ for black), see Figure 13.

In order to fix the up or down orientations of the $2N$ vertices, we split the sequence $(1, 2, \ldots, 2N)$ into two increasing subsequences V_{up} and V_{down}. We then read along the line the colors of the up vertices $C_{up} = \mathrm{Col}(V_{up})$ (with, formally, Col the operator acting on a sequence $V = (v_i)_i$ and returning the sequence $C = \mathrm{Col}(V) := (\mathrm{col}(v_i))_i$) and do the same for $C_{down} = \mathrm{Col}(V_{down})$. The number of bicolored arch systems compatible with the choice of orientation (V_{up}, V_{down}) is factorized into $a(C_{up})a(C_{down})$ where $a(C)$ is defined as the number of bicolored arch systems on *one side* of the line (up and down are clearly equivalent) compatible with the color sequence C (see Figure 13).

To get the total number of Hamiltonian cycles z_N, we have to sum over all possible partitions (V_{up}, V_{down}), hence:

$$z_N = \sum_{V_{up}} a(\mathrm{Col}(V_{up}))a(\mathrm{Col}(V_{down})) \ . \tag{40}$$

Non-zero contributions to this sum correspond to *admissible* sequences V_{up} with equal numbers of black and white vertices, which automatically implies the same property for V_{down}.

Denote by k the number of (white/black) vertex pairs in V_{up}. As we have to choose k black vertices among N and k white vertices among N, the number of admissible partitions to deal with is

$$\sum_{k=0}^{N} \binom{N}{k}^2 = \binom{2N}{N} \sim \frac{4^N}{\sqrt{\pi N}} \ . \tag{41}$$

The computer time therefore increases exponentially with N, which in practice rapidly limits the accessible values of N. One may try to accelerate the program, for instance by
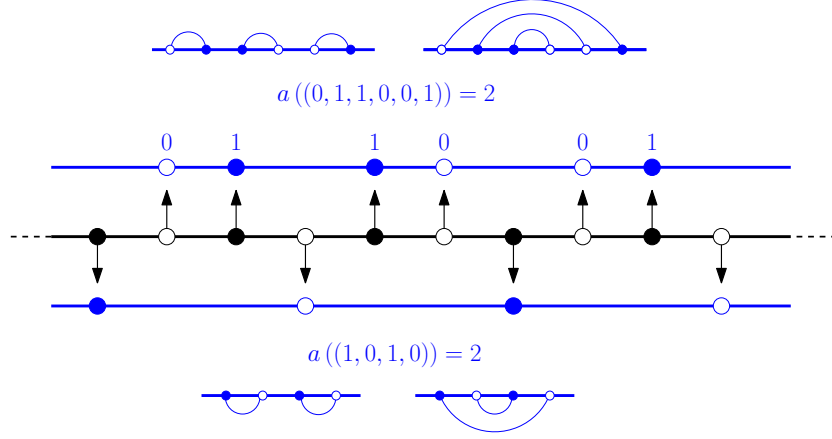
Figure 13: Illustration of the up-down factorization method, here for $2N = 10$ vertices. We first split the vertex sequence into complementary sequences $V_{up} = (2, 3, 5, 6, 8, 9)$ of up-oriented vertices and $V_{down} = (1, 4, 7, 10)$, with associated color sequences $C_{up} = (0, 1, 1, 0, 0, 1)$ and $C_{down} = (1, 0, 1, 0)$. There are $a(C_{up}) = 2$ configurations of unisided bicolored arches as shown. We also have $a(C_{down}) = 2$ so that there are $2 \times 2 = 4$ arch systems compatible with this choice of vertex orientations.

using a "memoization technique" which consists in storing the values of $a(C)$ whenever we encounter the sequence C for the first time so that we do not have to compute it again at a later occurrence of C. But we are then limited by memory size, since the method requires the storage of $O(4^N)$ correspondences $(C, a(C))$.

5.2. Enumeration results

Let us describe the various configuration ensembles that we have enumerated. In all the definitions below, it is understood that an arch always connects a black and a white vertex and that the straight line is implicitly oriented from left to right.

Hamiltonian cycles Our first combinatorial quantity is the number z_N of Hamiltonian cycles on planar bicubic maps, as defined earlier, with $2N$ vertices and with an extra marked visited (root) edge. In the arch language, we may write pictorially
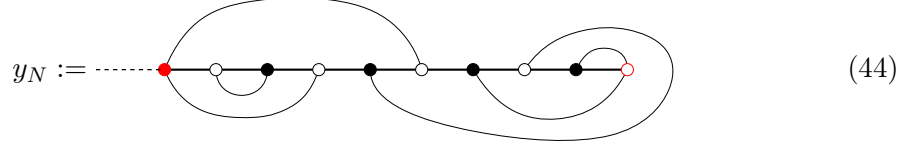
$$z_N := \qquad\qquad\qquad\qquad\qquad\qquad\qquad (42)$$

with an *infinite line* carrying $2N$ alternating black and white vertices, and with a total of N non-crossing arches. We have obtained the first values of z_N independently by the transfer matrix and by the up-down factorization methods, allowing for a cross-check of the results. We find:

$$(z_N)_{N \geq 1} = (2, 8, 40, 228, 1424, \ldots) . \qquad\qquad\qquad (43)$$

21

The complete list up to $N = 28$ is given in Table 2 of Appendix B. It confirms and extends the results of [1] (limited to $N \leq 20$), see also the sequence A116456 in OEIS [35].

Hamiltonian open paths with trivalent endpoints The second quantity that we considered is the number y_N of Hamiltonian *open* paths on planar bicubic maps with $2N + 2$ vertices (in particular, the endpoints of the path are trivalent). As already seen in the regular lattice case, the endpoints of the path correspond to defects with opposite magnetic charges $\pm M$, with $M = 2A + B = \frac{3}{2}A + \frac{1}{2}b_2$. In the arch language, we may write pictorially

$$y_N := \quad\text{-------}\quad \tag{44}$$
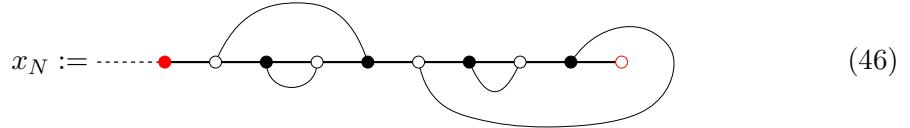
with a now a *line segment* of $2N + 2$ alternating black and white vertices and a total of $N + 2$ non-crossing arches. In the planar representation of the map, we fixed as *external face* that containing the corner between the two unvisited edges at the black endpoint (marked here by a dashed segment – this de facto allows us to extend the line segment into an infinite half-line). The arches are now allowed to wind around the line segment by passing to the right of the white endpoint. We obtained the first values of y_N independently by the transfer matrix and by the up-down factorization methods:

$$(y_N)_{N \geq 0} = (1, 6, 40, 286, 2152, \ldots) \ . \tag{45}$$

The complete list up to $N = 16$ is given in Table 3 of Appendix B.

Hamiltonian open paths with univalent endpoints The third quantity of interest is the number x_N of Hamiltonian open paths on planar bicolored maps with $2N$ trivalent vertices and 2 univalent ones. There the path necessarily starts and ends at the two univalent vertices which moreover correspond to defects with opposite magnetic charges $\pm M$ with now $M = B = -\frac{1}{2}A + \frac{1}{2}b_2$. In the arch language, we have pictorially

$$x_N := \quad\text{-------}\quad \tag{46}$$

with a line segment of $2N + 2$ alternating black and white vertices and a total of N non-crossing arches connecting all vertices except the two extremal ones. In the planar representation of the map, we took as external face that containing the corner at the univalent black vertex so that the arches are allowed to wind around the line segment by passing to the right of the white univalent vertex. We obtained the first values of x_N independently by the transfer matrix and by the up-down factorization methods:

$$(x_N)_{N \geq 0} = (1, 4, 24, 168, 1280, \ldots) \ . \tag{47}$$

The complete list up to $N = 17$ is given in Table 4 of Appendix B.

The following ensembles correspond to "vacancy defects", i.e. configurations having two or three *unvisited vertices*.

Hamiltonian cycles with two unvisited univalent vertices   The fourth quantity which we studied is the number $2w_N$ of cycles on planar bicolored maps with $2N$ trivalent vertices and 2 univalent ones, such that the cycle visits all the trivalent vertices but, since it is a cycle, cannot visit the univalent ones (which are then necessarily of different colors). This situation corresponds to having two defects with opposite magnetic charges $\pm M$ with $M = A$. In the arch language, we have pictorially

$$w_N := \frac{1}{2} \times \qquad\qquad\qquad\qquad\qquad\qquad\qquad\qquad\qquad\qquad \tag{48}$$

with an infinite line carrying $2N$ alternating white and black vertices, a black univalent vertex grafted above the first (white) vertex of the line and a white univalent vertex grafted above or below one of the black vertices of the line. The configuration now has a total of $N-1$ non-crossing arches. In the planar representation of the map, we took as external face that containing the corner at the univalent black vertex. The factor $\frac{1}{2}$ is because we factored out the trivial symmetry consisting in flipping up or down the univalent white vertex. The first values of w_N were obtained independently by the transfer matrix method and by the up-down factorization method, with result:

$$(w_N)_{N\geq 1} = (1, 4, 22, 140, 972, \dots) \ . \tag{49}$$

The complete list up to $N = 18$ is given in Table 5 of Appendix B.

Hamiltonian cycles with two unvisited bivalent vertices   Our fifth quantity is the number v_N of cycles on planar bicolored maps with $2N$ trivalent vertices and 2 bivalent ones (which are then necessarily of different color), where we require that the cycle visits all the trivalent vertices but *not the bivalent ones*. This situation corresponds to having two defects with opposite magnetic charges $\pm M$ with $M = 2A$. In the arch language, we have pictorially

$$v_N := \qquad\qquad\qquad\qquad\qquad\qquad\qquad\qquad\qquad\qquad\qquad \tag{50}$$

with an infinite line carrying $2N$ alternating white and black vertices, a black bivalent vertex linked (from above) to two (white) vertices of the line among which we choose the first white vertex along the line, and a white bivalent vertex linked to two black vertices of the line. The configuration has $N-2$ additional non-crossing arches. The two edges incident to the bivalent black vertex are distinguished as e_1 and e_2 and, in the planar representation of the map, we take as external face that containing the corner

between edges e_1 and e_2 clockwise. The first values of v_N were obtained by the up-down factorization method, with result:

$$(v_N)_{N \geq 2} = (1, 10, 84, 682, 5534, \ldots) \ . \tag{51}$$

The complete list up to $N = 21$ is given in Table 6 of Appendix B.

Hamiltonian cycles with two univalent one bivalent unvisited vertices   The last quantity which we considered is the number $4u_N$ of cycles on planar bicolored maps with $2N$ trivalent vertices, 1 bivalent black one and 2 univalent white ones, such that the cycle visits all the trivalent vertices but not the bivalent or univalent ones. This situation corresponds to having *three defects* with respective magnetic charges $2\boldsymbol{A}$, $-\boldsymbol{A}$ and $-\boldsymbol{A}$. In the arch language, we have pictorially

$$u_N := \frac{1}{4} \times \tag{52}$$

with an infinite line carrying $2N$ alternating white and black vertices, a black bivalent vertex linked (from above) to two (white) vertices of the line among which we choose the first white vertex along the line, and two white univalent vertices grafted to black vertices along the line. The configuration has $N - 2$ additional non-crossing arches. Again, the two edges incident to the bivalent black vertex are distinguished as e_1 and e_2 and, in the planar representation of the map, we take as external face that containing the corner between edges e_1 and e_2 clockwise. The factor $\frac{1}{4}$ is because we factored out the trivial symmetry consisting in flipping up or down the univalent white vertices. The first values of u_N were obtained by the up-down factorization method, with result:

$$(u_N)_{N \geq 2} = (1, 10, 90, 798, 7094, \ldots) \ . \tag{53}$$

The complete list up to $N = 17$ is given in Table 7 of Appendix B.

5.3. Exponential growth rate

All the quantities $t_N = z_N, y_N, x_N, w_N, v_N, u_N$ which we introduced so far are expected to have the asymptotic behavior

$$t_N \sim \text{const.} \frac{\mu^{2N}}{N^{\beta_t}} \ , \tag{54}$$

with *the same* exponential growth rate μ and sub-leading corrections characterized by an exponent β_t *specific to each quantity* and whose value should be predicted from the KPZ formulas. In order to evaluate μ and β_t, we construct from the sequence t_N the following two sequences

$$a_N := \frac{t_{N+1}}{t_N} \ , \qquad b_N := N^2 \text{Log} \frac{t_{N+2} t_N}{(t_{N+1})^2} \ , \tag{55}$$

24

which are such that

$$a_N \underset{N\to\infty}{\to} \mu^2 , \qquad b_N \underset{N\to\infty}{\to} \beta_t . \tag{56}$$

To improve our estimates, we have recourse to two *series acceleration methods*, used for accelerating the rate of convergence of our sequences above. Both are expressed via the iterated finite difference operators Δ^k, $k \in \mathbb{N}^*$, defined by

$$\begin{aligned}
(\Delta f)_N &:= f_{N+1} - f_N , \\
(\Delta^2 f)_N &:= (\Delta(\Delta f))_N = f_{N+2} - 2f_{N+1} + f_N , \ \ldots
\end{aligned} \tag{57}$$

The first method considers the sequences

$$\tilde{a}_N^{(k)} := \frac{1}{k!}\left(\Delta^k \hat{a}^{(k)}\right)_N \quad \text{with} \quad \hat{a}_N^{(k)} := N^k a_N \tag{58}$$

and similarly defined sequences $\tilde{b}^{(k)}$. The convergence of these sequences to μ^2 and β_t is faster for increasing k even though, in practice, since we know t_N for the first values of N only, we cannot go to k larger that 7 or so.

The second method is the so-called Aitken-Δ^2 method which considers sequences defined recursively via

$$\bar{a}_N^{(k)} := \bar{a}_N^{(k-1)} - \frac{k+1}{k}\frac{\left(\Delta \bar{a}^{(k-1)}\right)_N \left(\Delta \bar{a}^{(k-1)}\right)_{N-1}}{\left(\Delta^2 \bar{a}^{(k-1)}\right)_{N-1}} \quad \text{with} \quad \bar{a}_N^{(0)} := a_N \tag{59}$$

and similarly defined sequences $\bar{b}^{(k)}$. Again, the convergence of these sequences is faster for increasing k (in practice we use $k = 1, 2$ and 3).

Estimate of μ from the sequence z_N. Figure 14 shows our estimates for μ^2 obtained from our data z_N for the numbers of Hamiltonian cycles. More precisely, it displays the sequences $\tilde{a}^{(k)}$ for $k = 3, 5, 7$ and $\bar{a}^{(k)}$ for $k = 1, 2, 3$ using the sequence $a_N = z_{N+1}/z_N$ as original input. We estimate from these data

$$\mu^2 = 10.113 \pm 0.001 , \tag{60}$$

so that $\text{Log}(\mu^2) = 2.3138 \pm 0.0001$, in agreement with [1].

Estimate of μ from other observables. We then compared this value of μ with that obtained from the other sequences $y_N, x_N, \ldots, u_N$ corresponding to the enumerations of the various Hamiltonian path configurations with defects introduced in the previous section. Figure 15 shows the values of μ^2 obtained from the sequences $\tilde{a}^{(3)}(t)$ obtained via (58) for $a_N = t_{N+1}/t_N$ with $t_N = y_N, x_N, \ldots, u_N$ and compare them with that obtained previously for $t_N = z_N$. As expected, all estimates converge to the *same value* of μ, which is a non-trivial test of the consistency of our data for the various sequences.
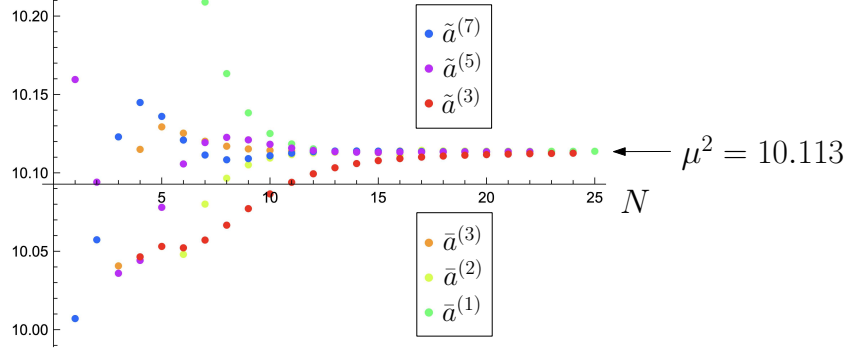
Figure 14: Estimate of μ^2 from the sequences $\tilde{a}^{(k)}$ for $k = 3, 5, 7$ and the sequences $\bar{a}^{(k)}$ for $k = 1, 2, 3$ as defined via (58) and (59) with $a_N = z_{N+1}/z_N$.
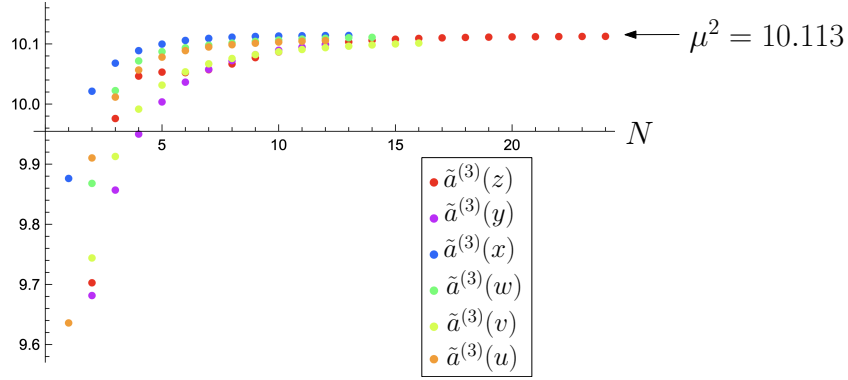

Figure 15: Estimate of μ^2 from the sequences $\tilde{a}^{(3)}(t)$ as defined via (58) for $a_N = t_{N+1}/t_N$ and $t_N = z_N, y_N, \ldots, u_N$.

5.4. Exponents

Let us now present our numerical estimates for the various exponents β_z, β_y, β_x, β_w, β_v and β_u as defined by (54) with $t_N = z_N$, y_N, x_N, w_N, v_N and u_N respectively. Figure 16 shows for instance the estimate $\beta_y = 1.90 \pm 0.01$ deduced from the sequences $\tilde{b}^{(k)}$ for $k = 4, 5, 6$ and $\bar{b}^{(k)}$ for $k = 2, 3$ with $b_N = N^2 \mathrm{Log}(y_{N+2}y_N/(y_{N+1})^2)$ as input. Repeating this analysis with our numerical data for the various sequences leads to

$$\begin{aligned} \beta_z &= 2.77 \pm 0.01 \,, & \beta_y &= 1.90 \pm 0.01 \,, & \beta_x &= 1.19 \pm 0.01 \,, \\ \beta_w &= 1.99 \pm 0.01 \,, & \beta_v &= 2.38 \pm 0.03 \,, & \beta_u &= 1.32 \pm 0.02 \,. \end{aligned} \tag{61}$$

Here the announced values correspond to the *stable* digits in $\left(\tilde{b}^{(k)}\right)_{N_{max}^{(k)}}$ for the largest accessible value of $N_{max}^{(k)}$ at a given k, i.e., those digits which do not vary when going from $N_{max}^{(k)} - 1$ to $N_{max}^{(k)}$ nor by increasing k by 1. This implicitly assumes that we have already reached the asymptotic regime for $N \sim N_{max}^{(k)}$. From our data, this condition is not satisfied for β_v and its value announced above is probably slightly underestimated.
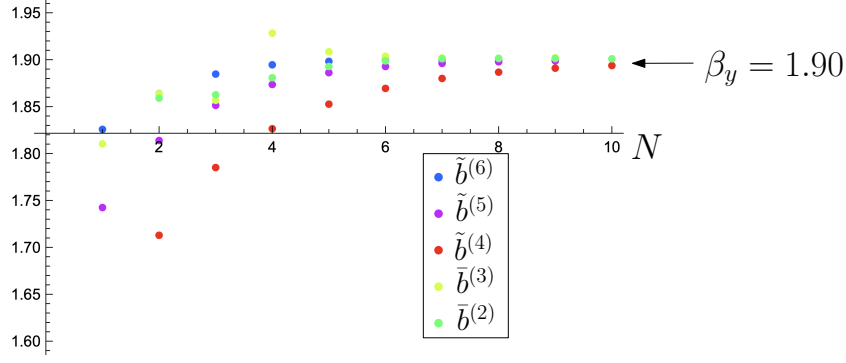
26

Figure 16: Estimate of β_y from the sequences $\tilde{b}^{(k)}$ for $k = 4, 5, 6$ and the sequences $\bar{b}^{(k)}$ for $k = 2, 3$ with $b_N = N^2 \mathrm{Log}(y_{N+2} y_N / (y_{N+1})^2)$.

We will come back to this point in the next section. As for the indicated error ranges, they are estimated from the observed amplitude for the variation of the first digit which is not yet stabilized.

6. Comparison with KPZ predictions

We now wish to compare the numerical exponents above to their values predicted by the KPZ equivalence. Since we expect that $c = c_{\mathrm{fpl}}(0) = -1$ for $n = 0$ ($g = \frac{1}{2}$), we have, from (21), the exponent

$$\gamma := \gamma(-1) = -\frac{1 + \sqrt{13}}{6} = -0.76759\ldots \tag{62}$$

and, from (23), the gravitational anomalous dimensions

$$\Delta_{\boldsymbol{M}} := \Delta(h_{\boldsymbol{M}}, -1) = \frac{\sqrt{1 + 12 h_{\boldsymbol{M}}} - 1}{\sqrt{13} - 1} , \tag{63}$$

with, from (15) at $n = 0$ ($g = \frac{1}{2}$),

$$h_{\boldsymbol{M}} = \frac{1}{24}\phi_1^2 + \frac{1}{8}\left(1 - \delta_{\phi_2,0}\right)\left(\phi_2^2 - 1\right) \qquad \text{for} \quad \boldsymbol{M} = \phi_1 \boldsymbol{A} + \phi_2 \boldsymbol{b_2} . \tag{64}$$

From the general formulas (22) and (25) and the identity $h_{-\boldsymbol{M}} = h_{\boldsymbol{M}}$, hence $\Delta_{-\boldsymbol{M}} = \Delta_{\boldsymbol{M}}$, we may write

$$
\begin{aligned}
&\beta_z = 2 - \gamma , &&\beta_y = 1 + 2\Delta_{\frac{3}{2}\boldsymbol{A}+\frac{1}{2}\boldsymbol{b_2}} - \gamma , &&\beta_x = 1 + 2\Delta_{-\frac{1}{2}\boldsymbol{A}+\frac{1}{2}\boldsymbol{b_2}} - \gamma , \\
&\beta_w = 1 + 2\Delta_{\boldsymbol{A}} - \gamma , &&\beta_v = 1 + 2\Delta_{2\boldsymbol{A}} - \gamma , &&\beta_u = \Delta_{2\boldsymbol{A}} + 2\Delta_{\boldsymbol{A}} - \gamma .
\end{aligned} \tag{65}
$$

As in [1], our estimated value $\beta_z = 2.77 \pm 0.01$ above is in perfect agreement with the announced value $2 - \gamma = 2.76759\ldots$ and we thus confirm the prediction (2) of [1].

27

Before going to the precise values of the other exponents, we note that we have from (65) the consistency relation

$$2\beta_u - \beta_v = 2\beta_w + \gamma - 3 . \tag{66}$$

Assuming now that γ is indeed determined by (62), this relation provides a cross check between, on the one hand, our numerical estimates for β_u and β_v and, on the other hand, the estimate for $2\beta_u - \beta_v$ inherited from the estimate (61) for β_w. As displayed in Figure 17, these three estimates are indeed consistent with each other. As mentioned above, we are however not fully confident with our estimated range of β_v. The relation (66) may then be used to determine the value of β_v from those of β_u and β_w. If we do so, this leads us to reevaluate the estimate for β_v as $\beta_v = 2.42 \pm 0.06$, see Figure 17.
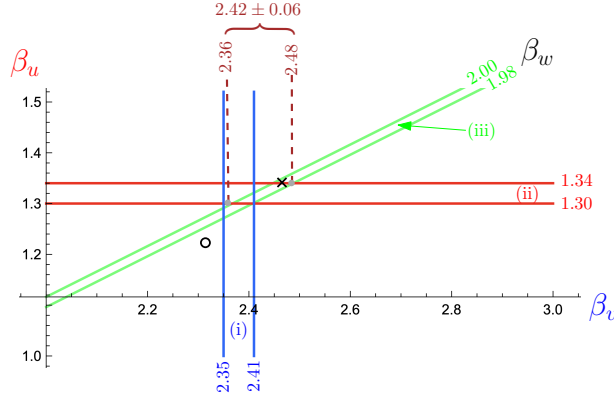

Figure 17: Consistency between the estimated value of β_v (domain (i) between the two vertical blue lines), that of β_u (domain (ii) between the two horizontal red lines) and that of the combination $2\beta_u - \beta_v$ (domain (iii) between the two diagonal lines) as obtained from the relation (66) and the estimated range (61) for β_w. The three domains do indeed share a common sector in the (β_v, β_u) plane. In the absence of a direct estimate (i) for β_u, we would predict from the intersection of domains (ii) and (iii) only a somewhat larger domain $\beta_v = 2.42 \pm 0.06$ (dashed brown lines). The $\circ$ symbol indicates the prediction of the naive KPZ formulas while the $\times$ symbol indicates that of the $(4/3)$-corrected KPZ formulas, see text.

Let us now come to the prediction for the exponents $\beta_y, \beta_x, \dots \beta_u$ themselves. As displayed in Table 1, we find without any doubt that the "naive" prediction (63)-(65) above *does not match* with our numerical results. However, a reasonable agreement may again be recovered if, as done in Section 4 for $n = 1$, we perform a modification of $\Delta_{\boldsymbol{M}}$ into

$$\Delta_{\boldsymbol{M}} := \Delta(h_{\boldsymbol{M}}^{(\alpha)}, -1) = \frac{\sqrt{1 + 12h_{\boldsymbol{M}}^{(\alpha)}} - 1}{\sqrt{13} - 1} , \tag{67}$$

with $h_{\boldsymbol{M}}^{(\alpha)}$ defined as in (35), now for $n = 0$, that is

$$h_{\boldsymbol{M}}^{(\alpha)} = \frac{\alpha}{24}\phi_1^2 + \frac{1}{8}\left(1 - \delta_{\phi_2,0}\right)\left(\phi_2^2 - 1\right) \qquad \text{for} \quad \boldsymbol{M} = \phi_1\boldsymbol{A} + \phi_2\boldsymbol{b_2} \tag{68}$$

	numerics	naive KPZ ($\alpha = 1$)	(4/3)-corrected KPZ
β_z	2.77 ± 0.01	$\frac{1}{6}\left(13 + \sqrt{13}\right) = 2.76759\ldots$	$\frac{1}{6}\left(13 + \sqrt{13}\right) = 2.76759\ldots$
β_y	1.90 ± 0.01	$\frac{1}{6}\left(7 + \sqrt{13}\right) = 1.76759\ldots$	$1 + \frac{\sqrt{22}}{2\left(\sqrt{13}-1\right)} = 1.90008\ldots$
β_x	1.19 ± 0.01	1	$1 + \frac{\sqrt{6}}{6\left(\sqrt{13}-1\right)} = 1.15668\ldots$
β_w	1.99 ± 0.01	$1 + \frac{\sqrt{6}}{\sqrt{13}-1} = 1.94010\ldots$	$1 + \frac{2\sqrt{15}}{3\left(\sqrt{13}-1\right)} = 1.99096\ldots$
β_v	$2.38 \pm 0.03^{(*)}$	$1 + \frac{2\sqrt{3}}{\sqrt{13}-1} = 2.32951\ldots$	$1 + \frac{2\sqrt{33}}{3\left(\sqrt{13}-1\right)} = 2.46983\ldots$
β_u	1.32 ± 0.02	$\frac{\sqrt{3}+\sqrt{6}-1}{\sqrt{13}-1} = 1.22106\ldots$	$\frac{2\sqrt{15}+\sqrt{33}-3}{3\left(\sqrt{13}-1\right)} = 1.34207\ldots$

Table 1: Comparison of the numerical estimates for the various configuration exponents and their values predicted by the naive and by the (4/3)-corrected KPZ formulas. $^{(*)}$As explained in the text and in Figure 17, a more reliable estimate is $\beta_v = 2.42 \pm 0.06$.

and for a suitable choice of α. Figure 18 displays the value of the "α-corrected" KPZ prediction for the various exponents for a varying value of α between 1 and 2. We see that, while the value $\alpha = 1$ (naive KPZ prediction) is clearly ruled out, a reasonable agreement may be obtained if we take $\alpha \sim 4/3$. The "(4/3)-corrected" KPZ predictions are listed in Table 1 for a direct comparison with numerics.
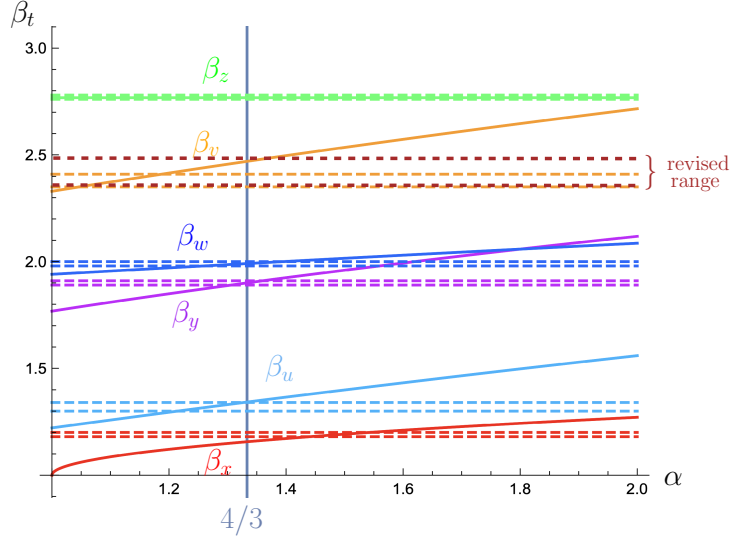

Figure 18: Comparison between the numerical estimates (dashed horizontal lines) of the various exponents and their "α-corrected" KPZ prediction (continuous lines) for α between 1 and 2. For β_v, we indicated in brown the revised extended range found in Figure 17. A reasonable matching is obtained for $\alpha \sim 4/3$.

7. Discussion

We have seen at the end of Section 4 that for the FPL(1) model, the presence of a normalization factor $\alpha = 9/8$ proved necessary in the Coulomb gas formula (35) for $h_{\boldsymbol{M}}^{(\alpha)}$, in order to recover from the (inverse) KPZ formula the quantum gravity exponents Δ_ℓ of [34] given by (37). Similarly, the numerical study of Sections 5 and 6 showed that various numerical critical exponents associated with FPL(0) on random bicubic maps could be consistently obtained by KPZ via the introduction of a similar factor $\alpha \sim 4/3$ in (35). We shall here try to give a possible meaning to these observed values.

We may rewrite (35) as

$$h_{\boldsymbol{M}}^{(\alpha)} := \frac{g'}{12}\phi_1^2 + \frac{g}{4}\left(1 - \delta_{\phi_2,0}\right)\left(\phi_2^2 - \left(1 - g^{-1}\right)^2\right) \qquad \text{for} \quad \boldsymbol{M} = \phi_1\boldsymbol{A} + \phi_2\boldsymbol{b_2} , \quad (69)$$

by distinguishing two coupling constants,

$$g' := \alpha g, \quad g = 1 - e_0 = \frac{1}{\pi}\arccos\left(-\frac{n}{2}\right) . \quad (70)$$

This corresponds to decoupling the scales of the two fields ψ_1 and ψ_2 in the Coulomb gas action (9), and replacing there the Gaussian term by $\frac{1}{3}g'(\nabla\psi_1)^2 + g(\nabla\psi_2)^2$. It is noteworthy that the *Ansatz*,

$$\alpha = \frac{1}{1 - e_0^2} , \quad (71)$$

reproduces $\alpha = 9/8$ for $n = 1$ and $\alpha = 4/3$ for $n = 0$. In turn, it yields the coupling constant of the ψ_1 Gaussian free field,

$$g' := \frac{1}{1 + e_0} . \quad (72)$$

To the constrained FPL(n) model on the honeycomb lattice corresponds an unconstrained O(n) model [6, 7, 8], whose (stable) *dense* critical phase has the same CG coupling constant $g = 1 - e_0$, with $1/2 \le g \le 1$ for $n = -2\cos(\pi g) \in [0, 2]$, and a central charge

$$c(g) := 1 - 6\frac{(1 - g)^2}{g} , \quad (73)$$

such that $-2 \le c(g) \le 1$, see Figure 19. The associated (unstable) *dilute* critical phase of the same O(n) model has coupling constant $\tilde{g} := 1 + e_0 = 2 - g$, with $1 \le \tilde{g} \le 3/2$ [10], such that $n = -2\cos(\pi\tilde{g})$, but with a different central charge, $c(\tilde{g}) = 1 - 6(1 - \tilde{g})^2/\tilde{g}$, such that $0 \le c(\tilde{g}) \le 1$.

The coupling contant g' of Equation (72) then appears to be the *dual* value of $\tilde{g}$,

$$g' = \frac{1}{\tilde{g}} = \frac{1}{2 - g} . \quad (74)$$

Because of its range, $2/3 \le g' \le 1$, this CG coupling constant g' corresponds to the *dense* phase of *another* O(n') model, such that $n' = -2\cos(\pi g')$, but with the *same*

central charge as that of the dilute critical O(n) model since, as easily checked, we have $c(g') = c(\tilde{g})$. The geometrical interpretation of this *duality* is as follows [36, 15, 16]. In the scaling limit, the loops of the dense O(n') model are *non-simple* random paths of Hausdorff dimension $D' = 1 + (2g')^{-1}$ [10]; their *external perimeters* are *simple* critical lines of the dilute critical O(n) model, of Hausdorff dimension $\tilde{D} = 1 + (2\tilde{g})^{-1}$. These Hausdorff dimensions thus satisfy the (super-)universal duality relation $(D'-1)(\tilde{D}-1) = 1/4$ [36], which can be directly obtained in the case of critical percolation [37].

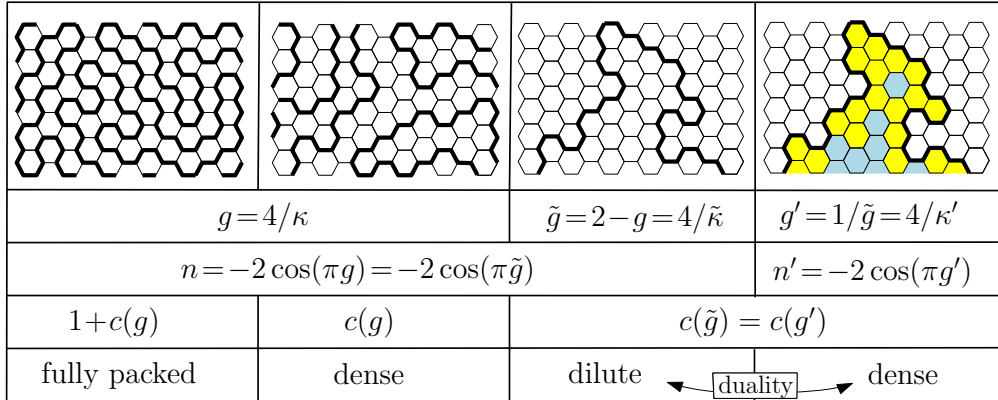|			
$g = 4/\kappa$		$\tilde{g} = 2 - g = 4/\tilde{\kappa}$	$g' = 1/\tilde{g} = 4/\kappa'$
$n = -2\cos(\pi g) = -2\cos(\pi\tilde{g})$			$n' = -2\cos(\pi g')$
$1 + c(g)$	$c(g)$	$c(\tilde{g}) = c(g')$	
fully packed	dense	dilute ←[duality]→ dense	

Figure 19: Illustration of the different loop models on the honeycomb lattice and their connections. We have $\frac{1}{2} \leq g \leq 1$, $1 \leq \tilde{g} \leq \frac{3}{2}$ and $\frac{2}{3} \leq g' \leq 1$. For $n = 0$, we have $g = \frac{1}{2}$ ($\kappa = 8$), $\tilde{g} = \frac{3}{2}$ ($\tilde{\kappa} = \frac{8}{3}$)), $g' = \frac{2}{3}$ ($\kappa' = 6$), hence $n' = 1$. For $n = 1$, we have $g = \frac{2}{3}$ ($\kappa = 6$), $\tilde{g} = \frac{4}{3}$ ($\tilde{\kappa} = 3$) $g' = \frac{3}{4}$ ($\kappa' = 16/3$), hence $n' = \sqrt{2}$. Top line from left to right, ($n = 0, n' = 1$) case: Hamiltonian walk, dense walk, SAW, SAW as the external perimeter of a percolation cluster.

This Coulomb gas $g \leftrightarrow 1/g$ "electro-magnetic" duality directly leads to the $\kappa \leftrightarrow 16/\kappa$ duality of Schramm-Loewner evolution SLE$_\kappa$ [36, 15, 16]. The CG coupling constant spans the range $g \in [1/2, 3/2]$ for the (dense and dilute) critical O(n) model (for $n \geq 0$), and the SLE parameter the range $\kappa = 4/g \in [8/3, 8]$ for its scaling limit, the conformal loop ensemble CLE$_\kappa$. When $\kappa \in (4, 8]$, SLE$_\kappa$ paths are non-simple [18], and their outer boundaries have been proven to be dual simple SLE$_{16/\kappa}$ paths, with $16/\kappa \in [2, 4)$ [38, 39].

To the fully-packed FPL($n = 1$) model considered in Section 4 above corresponds an unconstrained dense O($n = 1$) model with CG coupling constant $g = 2/3$ and central charge $c_{\text{dense}}(n = 1) = 0$, describing in particular critical percolation. The associated dilute phase has $\tilde{g} = 4/3$, which is associated with the critical Ising model of central charge $c = 1/2$. By duality, we find a second dense O($n' = \sqrt{2}$) model with coupling constant $g' = 3/4$, which also describes the Fortuin-Kasteleyn (FK) clusters of the critical $Q = 2$ Potts model. In terms of SLE$_\kappa$, critical percolation corresponds to $\kappa = 4/g = 6$ [20], the critical Ising model to $\tilde{\kappa} := 4/\tilde{g} = 3$ [21], while $Q = 2$ FK clusters generate dual SLE$_{16/3}$ random paths.

For the FPL($n = 0$) model describing Hamiltonian cycles and paths as studied in Sections 5 and 6, the corresponding unconstrained dense O($n = 0$) model is that of dense

polymers with $g = 1/2$, $c_{\text{dense}}(n = 0) = -2$; the dilute phase is then naturally that of critical self-avoiding walks (SAW), i.e., dilute polymers with $\tilde{g} = 3/2$ and $c = 0$. By duality, the associated final dense $O(n' = 1)$ model is that of percolation with $g' = 2/3$ and $c = 0$. In terms of SLE_κ, one here goes from $\kappa = 8$ to $\tilde{\kappa} = 8/3$ to $\kappa' = 6$, and it may be worth noting that in addition to critical percolation clusters [37, 40], planar Brownian loops also have the scaling limit of self-avoiding loops as external frontiers [41, 42, 43].

To conclude this discussion, while formulas (69) (70) and the Ansatz (71) (72) (74) seem appealing, and lead to connections between various critical statistical models that show up when using KPZ relations between fully-packed models on the honeycomb lattice and on random bicubic maps, it remains difficult at this stage to theoretically explain such apparent "transmutations" between models. Finally, let us remark that the observation that the usual KPZ relation (23) or (28) fails for a family of exponents of the fully-packed models may be linked to a *lack of independence* between some (constrained) configurations of the space-filling random paths and the random Liouville measure. Statistical independence is indeed crucial to the proof of that relation [24, 25]. The apparent enhancement of the effective coupling constant from g to $g' = 1/(2-g) \geq g$, for the extra Gaussian free field brought in by the full-packing condition, may reflect such a lack of independence.

Acknowledgements

A. Hamiltonian paths on random cubic maps

We discuss here briefly the problem of Hamiltonian path configurations defined on *cubic* planar maps. In practice, all the definitions given in Section 5.2 remain unchanged *except that we suppress the black/white colors of the vertices* and consequently forget about any bicoloration constraint whatsoever. In this way, we define new numbers $z_N^\circ, y_N^\circ, \ldots, u_N^\circ$ which are the analogs for cubic maps of the numbers $z_N, y_N, \ldots, u_N$. Note that all the maps which we consider have by construction an even number of trivalent vertices[3] so that the meaning of N is unchanged (e.g., there are $2N$ trivalent vertices in configurations enumerated by z_N°). We again define the exponential growth rate μ° and the configuration exponents β_t° via the large N behaviors

$$t_N^\circ \sim \text{const.} \frac{(\mu^\circ)^{2N}}{N^{\beta_t^\circ}} \tag{75}$$

---

[3] The number V_3 of trivalent vertices is even for all cubic maps with, possibly, an arbitrary number V_2 of bivalent defects and an *even* number V_1 of univalent ones since $3V_3 = 2E - 2V_2 - V_1$ where E is the number of edges.

for the various quantities at hand. It is a simple exercise to obtain the exact expression

$$z_N^\circ = \sum_{k=0}^{N} \binom{2N}{2k} \mathrm{Cat}_k \mathrm{Cat}_{N-k} = \mathrm{Cat}_N \mathrm{Cat}_{N+1} \ , \tag{76}$$

where $\mathrm{Cat}_N = \binom{2N}{N}/(N+1)$ is the Nth Catalan number. We similarly get

$$y_N^\circ = 2^{2N} \mathrm{Cat}_{N+2} \ , \qquad x_N^\circ = 2^{2N} \mathrm{Cat}_N \ , \qquad w_N^\circ = (2N-1)\mathrm{Cat}_{N-1}\mathrm{Cat}_N \ ,$$
$$v_N^\circ = \frac{1}{2}(N-1)\mathrm{Cat}_N\mathrm{Cat}_{N+1} \ , \qquad u_N^\circ = \frac{1}{4}(2N-1)(2N-2)\mathrm{Cat}_{N-1}\mathrm{Cat}_N \ . \tag{77}$$

From these exact expressions, we immediately obtain that all these sequences have the same exponential growth rate $(\mu^\circ)^2 = 16$, while the configuration exponents read:

$$\beta_z^\circ = 3 \ , \qquad \beta_y^\circ = \beta_x^\circ = \frac{3}{2} \ , \qquad \beta_w^\circ = \beta_v^\circ = 2 \qquad \beta_u^\circ = 1 \ . \tag{78}$$

These values match with the predictions

$$\beta_z^\circ = 2 - \gamma^\circ \ , \qquad \beta_y^\circ = 1 + 2\Delta_{\frac{3}{2}\boldsymbol{A} + \frac{1}{2}\boldsymbol{b_2}}^\circ - \gamma^\circ \ , \qquad \beta_x^\circ = 1 + 2\Delta_{-\frac{1}{2}\boldsymbol{A} + \frac{1}{2}\boldsymbol{b_2}}^\circ - \gamma^\circ \ ,$$

$$\beta_w^\circ = 1 + 2\Delta_{\boldsymbol{A}}^\circ - \gamma^\circ \ , \qquad \beta_v^\circ = 1 + 2\Delta_{2\boldsymbol{A}}^\circ - \gamma^\circ \ , \qquad \beta_u^\circ = \Delta_{2\boldsymbol{A}}^\circ + 2\Delta_{\boldsymbol{A}}^\circ - \gamma^\circ \ ,$$
$$\tag{79}$$

upon taking $\Delta_{\frac{3}{2}\boldsymbol{A}+\frac{1}{2}\boldsymbol{b_2}}^\circ = \Delta_{-\frac{1}{2}\boldsymbol{A}+\frac{1}{2}\boldsymbol{b_2}}^\circ = -1/4$, $\Delta_{\boldsymbol{A}}^\circ = \Delta_{2\boldsymbol{A}}^\circ = 0$ and $\gamma^\circ = -1$. The latter value is that predicted by the KPZ formula (21) since, as discussed in Section 3.1 $c = -2$ is the expected central charge when the FPL(0) model is defined on cubic planar maps, and $\gamma(-2) = -1$. As for the dressed dimensions Δ°, their values do not depend on the component along the $\boldsymbol{A}$ direction, which is compatible with the fact that we must set $\boldsymbol{A} = \boldsymbol{0}$: we are therefore left in practice with the two independent exponents $\Delta_{\frac{1}{2}\boldsymbol{b_2}}^\circ = -1/4$ and $\Delta_{\boldsymbol{0}}^\circ = 0$, corresponding respectively to the 1- and 2-leg watermelon exponents [44]. From the KPZ formula (23) which, at $c = -2$, reduces to

$$\Delta(h, -2) = \frac{\sqrt{1 + 8\,h} - 1}{2} \tag{80}$$

we identify

$$\Delta_{\frac{1}{2}\boldsymbol{b_2}}^\circ = \Delta(h_{\frac{1}{2}\boldsymbol{b_2}}^\circ, -2) \qquad \text{and} \qquad \Delta_{\boldsymbol{0}}^\circ = \Delta(h_{\boldsymbol{0}}^\circ, -2) \tag{81}$$

with the classical dimensions $h_{\frac{1}{2}\boldsymbol{b_2}}^\circ = -3/32$ and $h_{\boldsymbol{0}}^\circ = 0$ [44]. These values are two instances with $\phi_2 = 1/2$ and 0 respectively of the general formula (64), which when $\boldsymbol{A} = \boldsymbol{0}$, translates into

$$h_{\phi_2 \boldsymbol{b_2}}^\circ = \frac{1}{8}\left(1 - \delta_{\phi_2,0}\right)\left(\phi_2^2 - 1\right) \ . \tag{82}$$

To conclude, the obtained configuration exponents for the FPL(0) model defined on cubic planar maps are exactly those predicted by the KPZ formulas. This confirms that the discrepancies with KPZ found in this paper for *bicubic* maps are due to the existence of the extra dimension (along $\boldsymbol{A}$) in the problem.

B. Enumeration results

N	z_N	N	z_N
1	2	15	1103650297320
2	8	16	9450760284100
3	40	17	81696139565864
4	228	18	712188311673280
5	1424	19	6255662512111248
6	9520	20	55324571848957688
7	67064	21	492328039660580784
8	492292	22	4406003100524940624
9	3735112	23	39635193868649858744
10	29114128	24	358245485706959890508
11	232077344	25	3252243000921333423544
12	1885195276	26	29644552626822516031040
13	15562235264	27	271230872346635464906816
14	130263211680	28	2490299924154166673782584

Table 2: The number z_N of Hamiltonian cycles on planar bicubic maps with $2N$ vertices, and a marked visited edge.

N	y_N	N	y_N
0	1	9	80576316
1	6	10	698497236
2	40	11	6125241762
3	286	12	54248935624
4	2152	13	484629868212
5	16830	14	4362375489180
6	135632	15	39532218657398
7	1119494	16	360393965832256
8	9421536		

Table 3: The number y_N of open Hamiltonian paths on planar bicubic with $2N + 2$ vertices.

N	x_N	N	x_N
0	1	9	56959872
1	4	10	512093760
2	24	11	4652471904
3	168	12	42641120752
4	1280	13	393739429376
5	10288	14	3659068137088
6	85776	15	34193890019424
7	734448	16	321103772899152
8	6416912	17	3028414925849920

Table 4: The number x_N of open Hamiltonian paths on planar bicolored maps with 2 univalent vertices and $2N$ trivalent ones.

N	w_N	N	w_N
1	1	10	29734848
2	4	11	251955792
3	22	12	2165922244
4	140	13	18848640980
5	972	14	165764482320
6	7160	15	1471222986648
7	55068	16	13162929589308
8	437692	17	118606870664836
9	3570100	18	1075505940036672

Table 5: Table of w_N where $2w_N$ is the number of cycles visiting all the trivalent vertices on planar bicolored maps with 2 (unvisited) univalent vertices and $2N$ trivalent ones.

N	v_N	N	v_N
2	1	12	1996703248
3	10	13	17470889224
4	84	14	154096032108
5	682	15	1369014000682
6	5534	16	12242457072892
7	45330	17	110131946780584
8	375868	18	996123282195032
9	3155704	19	9054534704495656
10	26808852	20	82678808925578480
11	230230658	21	758122496862199740

Table 6: The number v_N of cycles visiting all the trivalent vertices on planar bicolored maps with 2 (unvisited) bivalent vertices and $2N$ trivalent ones. The bivalent vertices have necessarily different colors and the edges incident to the black one are distinguished.

N	u_N	N	u_N
2	1	10	47714564
3	10	11	439727448
4	90	12	4075738256
5	798	13	37971881232
6	7094	14	355404743524
7	63508	15	3340333168292
8	573056	16	31512818722844
9	5210640	17	298306803039300

Table 7: Table of u_N where $4u_N$ is the number of cycles visiting all the trivalent vertices on planar bicolored maps with 1 (unvisited) bivalent black vertex with distinguished incident edges, 2 (unvisited) univalent vertices and $2N$ trivalent ones.

References

[1] E. Guitter, C. Kristjansen, and J.L. Nielsen. Hamiltonian cycles on random Eulerian triangulations. *Nuclear Physics B*, 546(3):731–750, 1999.

[2] V.G. Knizhnik, A.M. Polyakov, and A.B. Zamolodchikov. Fractal structure of 2d—quantum gravity. *Modern Physics Letters A*, 03(08):819–826, 1988.

[3] P. Di Francesco, O. Golinelli, and E. Guitter. Meanders: exact asymptotics. *Nuclear Physics B*, 570(3):699–712, 2000.

[4] P. Di Francesco, E. Guitter, and J.L. Jacobsen. Exact meander asymptotics: a numerical check. *Nuclear Physics B*, 580(3):757–795, 2000.

[5] P. Di Francesco and E. Guitter. Geometrically constrained statistical systems on regular and random lattices: From folding to meanders. *Physics Reports*, 415(1):1–88, 2005.

[6] H. W. J. Blöte and B. Nienhuis. Fully packed loop model on the honeycomb lattice. *Phys. Rev. Lett.*, 72:1372–1375, Feb 1994.

[7] M. T. Batchelor, J. Suzuki, and C. M. Yung. Exact results for Hamiltonian walks from the solution of the fully packed loop model on the honeycomb lattice. *Phys. Rev. Lett.*, 73:2646–2649, Nov 1994.

[8] Jane Kondev, Jan de Gier, and Bernard Nienhuis. Operator spectrum and exact exponents of the fully packed loop model. *Journal of Physics A General Physics*, 29, 03 1996.

[9] T. Dupic, B. Estienne, and Y. Ikhlef. Three-point functions in the fully packed loop model on the honeycomb lattice. *Journal of Physics A: Mathematical and Theoretical*, 52(20):205003, apr 2019.

[10] Bernard Nienhuis. Critical behavior of two-dimensional spin models and charge asymmetry in the Coulomb gas. *J. Stat. Phys.*, 34:731–762, 1984.

[11] F. David. Conformal field theories coupled to 2-d gravity in the conformal gauge. *Modern Physics Letters A*, 03(17):1651–1656, 1988.

[12] Jacques Distler and Hikaru Kawai. Conformal field theory and 2d quantum gravity. *Nuclear Physics B*, 321(2):509–527, 1989.

[13] Oded Schramm. Scaling limits of loop-erased random walks and uniform spanning trees. *Israel J. Math.*, 118:221–288, 2000.

[14] Scott Sheffield. Exploration trees and conformal loop ensembles. *Duke Mathematical Journal*, 147(1):79 – 129, 2009.

[15] Bertrand Duplantier. Higher conformal multifractality. *J. Statist. Phys.*, 110(3-6):691–738, 2003.

[16] B. Duplantier. Conformal fractal geometry & boundary quantum gravity. In M. L. Lapidus and M. van Frankenhuysen, editors, *Fractal geometry and applications: a jubilee of Benoît Mandelbrot, Part 2*, volume 72 of *Proc. Sympos. Pure Math.*, pages 365–482. Amer. Math. Soc., Providence, RI, 2004.

[17] Wouter Kager and Bernard Nienhuis. A guide to stochastic Löwner evolution and its applications. *J. Stat. Phys.*, 115(5-6):1149–1229, 2004.

[18] Steffen Rohde and Oded Schramm. Basic properties of SLE. *Ann. of Math. (2)*, 161(2):883–924, 2005.

[19] Oded Schramm and Scott Sheffield. Contour lines of the two-dimensional discrete Gaussian free field. *Acta Mathematica*, 202(1):21 – 137, 2009.

[20] Stanislav Smirnov. Critical percolation in the plane: conformal invariance, Cardy's formula, scaling limits. *Comptes Rendus de l'Académie des Sciences - Series I - Mathematics*, 333(3):239–244, 2001.

[21] Stanislav Smirnov. Conformal invariance in random cluster models. I: Holomorphic fermions in the Ising model. *Ann. Math. (2)*, 172(2):1435–1467, 2010.

[22] Dmitry Chelkak and Stanislav Smirnov. Universality in the 2d Ising model and conformal invariance of fermionic observables. *Invent. Math.*, 189(3):515 – 580, 2012.

[23] Jason Miller and Scott Sheffield. Imaginary geometry. IV: Interior rays, whole-plane reversibility, and space-filling trees. *Probab. Theory Relat. Fields*, 169(3-4):729–869, 2017.

[24] B. Duplantier and S. Sheffield. Liouville Quantum Gravity and KPZ. *Invent. Math.*, 185:333–393, 2011.

[25] B. Duplantier and S. Sheffield. Duality and KPZ in Liouville Quantum Gravity. *Phys. Rev. Lett.*, 102:150603, 2009.

[26] R. Rhodes and V. Vargas. KPZ formula for log-infinitely divisible multifractal random measures. *ESAIM: Probability and Statistics*, 15:358–371, 2011.

[27] Bertrand Duplantier, Rémi Rhodes, Scott Sheffield, and Vincent Vargas. Renormalization of critical Gaussian multiplicative chaos and KPZ relation. *Commun. Math. Phys.*, 330(1):283 – 330, 2014.

[28] Scott Sheffield. Conformal weldings of random surfaces: SLE and the quantum gravity zipper. *Ann. Probab.*, 44(5):3474 – 3545, 2016.

[29] B. Duplantier and S. Sheffield. Schramm-Loewner Evolution and Liouville Quantum Gravity. *Phys. Rev. Lett.*, 107:131305, 2011.

[30] Bertrand Duplantier, Jason Miller, and Scott Sheffield. Liouville Quantum Gravity as a mating of trees. *Astérisque.*, 427:1–258, 2021.

[31] Jacopo Borga, Ewain Gwynne, and Xin Sun. Permutons, meanders, and SLE-decorated Liouville quantum gravity. *arXiv:2207.02319 [math.PR]*, 2022.

[32] P. Di Francesco, E. Guitter, and C. Kristjansen. Fully packed $O(n = 1)$ model on random Eulerian triangulations. *Nuclear Physics B*, 549(3):657–667, 1999.

[33] Vladimir A. Kazakov and Paul Zinn-Justin. Two-matrix model with $ABAB$ interaction. *Nuclear Physics B*, 546(3):647–668, 1999.

[34] Ivan Kostov. Exact solution of the six-vertex model on a random lattice. *Nuclear Physics*, 575:513–534, 2000.

[35] The OEIS Foundation Inc. The on-line encyclopedia of integer sequences, published electronically at http://oeis.org, 2022.

[36] Bertrand Duplantier. Conformally invariant fractals and potential theory. *Phys. Rev. Lett.*, 84(7):1363–1367, 2000.

[37] Michael Aizenman, Bertrand Duplantier, and Amnon Aharony. Path-crossing exponents and the external perimeter in 2d percolation. *Phys. Rev. Lett.*, 83:1359–1362, 1999.

[38] Dapeng Zhan. Duality of chordal SLE. *Invent. Math.*, 174(2):309–353, 2008.

[39] Julien Dubédat. Duality of Schramm-Loewner evolutions. *Ann. Sci. Éc. Norm. Supér. (4)*, 42(5):697–724, 2009.

[40] B. Duplantier. Harmonic measure exponents for two-dimensional percolation. *Phys. Rev. Lett.*, 82:3940–3943, 1999.

[41] B. Duplantier. Two-dimensional copolymers and exact conformal multifractality. *Phys. Rev. Lett.*, 82:880–883, 1999.

[42] Gregory F. Lawler, Oded Schramm, and Wendelin Werner. The dimension of the planar Brownian frontier is 4/3. *Math. Res. Lett.*, 8(4):401–411, 2001.

[43] G.F. Lawler, O. Schramm, and W. Werner. On the scaling limit of planar self-avoiding walk. In M. L. Lapidus and M. van Frankenhuysen, editors, *Fractal geometry and applications: a jubilee of Benoît Mandelbrot, Part 2*, volume 72 of *Proc. Sympos. Pure Math.*, pages 339–364. Amer. Math. Soc., Providence, RI, 2004.

[44] Bertrand Duplantier and Ivan Kostov. Conformal spectra of polymers on a random surface. *Phys. Rev. Lett.*, 61:1433–1437, 1988.